Chapter 5
Application of Functional Molecular Imaging in Radiation Oncology

Sarwat Naz, Murali C. Krishna, and James B. Mitchell

Abstract Molecular imaging of tumors is rapidly gaining momentum as a tool with the capacity to improve cancer treatment. It has the potential to provide more precise diagnosis of cancer, improve radiation treatment planning, and monitor response to treatment as the treatment progresses. Noninvasive imaging platforms reporting on molecular, biochemical, metabolic, and physiological parameters coupled with existing high-resolution anatomical modalities hold the promise of providing clinicians with information regarding the *biology* of the tumor in the context of its anatomical location. The basic principles of established and emerging molecular imaging techniques as applied to radiation oncology are reviewed highlighting advantages and limitations. The application of molecular imaging monitoring normal tissue responses as well as tumor may provide a means to determine more precisely a therapeutic ratio of different experimental radiation or chemoradiation approaches.

Keywords Radiation oncology • Metabolic imaging • Functional imaging • Tumor heterogeneity • Molecular biomarker • Hypoxia • Glucose metabolism • PET/CT • ^{13}C hyperpolarization • Cell proliferation

Introduction

Radiation therapy is an effective non-invasive cancer therapy approach that can be administered to patients repetitively over a few to several weeks. Each year approximately 60 % of cancer patients, in the United States are given radiation therapy for definitive treatment, for palliation of symptoms, or as an adjunct to surgery or chemotherapy. A continuing challenge in the field of radiation oncology is to improve the therapeutic ratio, which is the balance of biological effectiveness of treatment and severity of treatment-related side effects on normal tissue. A major objective in

S. Naz • M.C. Krishna • J.B. Mitchell (✉)
Radiation Biology Branch, Center for Cancer Research, National Cancer Institute, National Institutes of Health, Bethesda, MD 20892, USA
e-mail: sarwat.naz@nih.gov; cherukum@mail.nih.gov; jbm@helix.nih.gov

P.J. Tofilon, K. Camphausen (eds.), *Increasing the Therapeutic Ratio of Radiotherapy*, Cancer Drug Discovery and Development,
DOI 10.1007/978-3-319-40854-5_5

radiation oncology is to accurately delineate tumor volume and thereby, when possible, minimize radiation exposure to normal tissues. In the past decade, substantial technological progress in radiation oncology has achieved remarkable success in radiation dose delivery with high geometric precision. This has been possible with the introduction of stereotactic radiotherapy, radiosurgery, intensity-modulated radiotherapy (IMRT), and three-dimensional planning of brachytherapy. Computer-optimized intensity-modulated radiation therapy (IMRT) allows achieving high radiation doses to the primary tumor while limiting the dose to radiation-sensitive normal tissues adjacent to the tumor. Despite the advancement in accurate delivery of high-dose radiotherapy, overall survival rates of some specific tumors have not significantly improved. There are several reasons behind this including intrinsic and acquired resistance of tumors mediated through genetic and phenotypic tumor heterogeneity and influence of the tumor microenvironment. Several clinical trials conducted using targeted therapies have demonstrated the existence of genetic and phenotypic tumor heterogeneity [1]. As a result, patients with similar tumor types exhibit differential responses to the same therapy. Genetic heterogeneity in a tumor can arise from the clonal expansion of aggressive and therapy-resistant cancer cells combined with spatial heterogeneity arising from variety of stresses imposed by the tumor microenvironment. These changes within a tumor can lead to regional differences in stromal composition [2], oxygen consumption and hypoxia [3, 4], glucose metabolism [4], and varied gene expression [5]. Consequently, subregions within a given tumor exhibit spatially distinct patterns of blood flow [6, 7], vessel permeability [8], cellular proliferation [9], cell death [10] and other related features. Spatial heterogeneity is observed between different tumors within individual patients (*intertumor heterogeneity*) and within each lesion in an individual (*intratumor heterogeneity*) patient. To overcome these barriers, additional approaches are warranted to quantitatively estimate the exact tumor volume and the extent of phenotypic tumor heterogeneity for effective delivery of ionizing radiation.

One approach to quantitatively extract information pertaining to tumor heterogeneity is the development and introduction of molecular imaging methods. Functional molecular imaging is a noninvasive approach providing visual and quantitative information about a disease process. In addition, it can be combined with diagnostic imaging modalities to provide spatial orientation that may provide molecular, biochemical, or physiological information unique to the tumor or region within the tumor. It is anticipated that such information will be of paramount importance in diagnosis, staging, and selection of tailored treatments and assessment of treatment response. Likewise, alterations in these functional endpoints may also prove useful in monitoring and predicting toxicities in treated normal tissues. Not only can these imaging modalities help to define a more precise "gross tumor volume" (GTV) but also can aid in establishing a "biological target volume" (BTV). The biological target volume represents a subregion within a given tumor with specific characteristics such as hypoxia [11]. Given the accuracy of modern radiation delivery instrumentations, such tumor volumes that are resistant to radiation could be given extra dose of radiation, thus enabling the concept of "dose painting" or "dose sculpturing" to be founded on firm biological and physiological rationale [12].

Combining functional molecular imaging with standard or experimental treatment approaches holds the promise to help clinicians rapidly assess the effectiveness of an existing or new therapy in individual patients and help abandon ineffective treatments at an early stage.

The emergence of functional molecular imaging modalities coupled with the availability of an expanding array of molecular probes is beginning to augment the role of molecular medicine in the treatment of cancer [13]. In this chapter, we briefly outline the basic principles of the different imaging modalities and discuss functional molecular imaging techniques to study functional characteristics of tumor mainly tumor glucose metabolism and hypoxia, application of molecular imaging in chemo-/radiotherapy planning, dose painting, and monitoring treatment response. We aim to discuss the limitations and challenges associated with individual imaging methods in preclinical and clinical setup. Lastly, we give an overall perspective on the future direction of this immensely growing field and its impact on image-guided radiotherapy.

Principles of Established and Emerging Advanced Molecular Imaging Technology

Medical imaging began with radiography after the discovery of X-rays in 1895 by Wilhelm Roentgen, a German professor of physics. X-rays were put to diagnostic use very early, before the dangers of ionizing radiation were discovered. Since then, imaging human diseases has advanced unprecedentedly. Various molecular imaging techniques exist at preclinical and clinical stages including magnetic resonance imaging (MRI), X-ray computed tomography (CT), positron emission topography (PET), ultrasound, and optical approaches. In this chapter, we describe specifically two widely used approaches, namely, MRI and PET, to image malignancies.

CT Imaging

X-ray computed tomography (CT) is a technique for visualizing interior features within solid objects. CT images can be generated by rotating a low-energy X-ray source and detector around the subject to acquire a series of projections. These projections are then used to construct a three-dimensional image. Contrast in the CT-generated image arises because of differential tissue absorption of X-rays. The main advantages of CT imaging are high spatial resolution (0.5–2.0 mm), fast acquisition time, simplicity, availability, and excellent hard-tissue imaging. CT imaging is being combined with PET, where it provides an anatomical context to the relatively low-resolution PET image. In the clinic, the fusion of X-ray CT and PET images has led to improvements in tumor detection.

Radionuclide Imaging

Radionuclide molecular imaging mainly includes positron-emitting tomography (PET) and single-positron emission CT (SPECT) imaging. Due to their high sensitivity and quantitative nature of acquiring images, radionuclide molecular imaging has played a significant role in advancing the preclinical and clinical studies [14]. We highlight some preclinical and clinical studies that have confirmed the feasibility of using radionuclide molecular imaging in cancer [15, 16].

PET and SPECT

Positron-emitting tomography (PET) and single-positron emission CT (SPECT) imaging are radionuclide-imaging techniques, which provide relatively low-resolution images of injected probe molecules that have been labeled with positron-emitting (PET) or γ-emitting isotopes (SPECT). The sensitivity of PET is in the picomolar range, facilitating investigation of biological processes without any adverse pharmacological effects from the labeled probe molecule, namely, ^{11}C, ^{15}O, ^{18}F, and ^{124}I [17]. PET can accurately assess the functional and biochemical processes of the body's tissues, before any detectable anatomical or structural changes have occurred. In the clinic, PET has been crucial for cancer detection and staging, as well as evaluation of response to therapy. An important advantage of PET over SPECT is that positron-emitting isotopes can be substituted for naturally occurring atoms in the probe compound without any effect on probe function. Over the past decade, with the progress of molecular biology and radiochemistry, a variety of PET tracers have been developed with high specificities and affinities. Several PET tracers have been characterized for their application in functional imaging of tumors preclinically and clinically. Among several PET radiotracers used for cancer imaging, ^{18}F-FDG is the most widely used and acceptable PET tracer. PET imaging lacks anatomical parameters to identify molecular events with accurate correlation to anatomical findings, and this disadvantage has been compensated by merging PET imaging with either CT or MR. PET/CT imaging can help to differentiate neoplastic areas with hypermetabolic activity within the surrounding normal tissue (Fig. 5.1) [18]. PET has become extremely useful to delineate the GTV for radiotherapy planning and monitoring treatment response.

Like PET, SPECT has also been extensively employed in the clinic. In general, SPECT isotopes have long half-lives, whereas PET isotopes have relatively short half-lives. Commonly used isotopes for SPECT imaging include [^{111}In] indium and [^{177}Lu] lutetium. Most importantly, SPECT can distinguish among different radioisotopes based on the isotope-specific energies of the emitted photons. Therefore, it is possible to image different targets simultaneously using SPECT [19]. In recent times, application of SPECT imaging in the clinic is less compared to MRI, PET, and ultrasound.

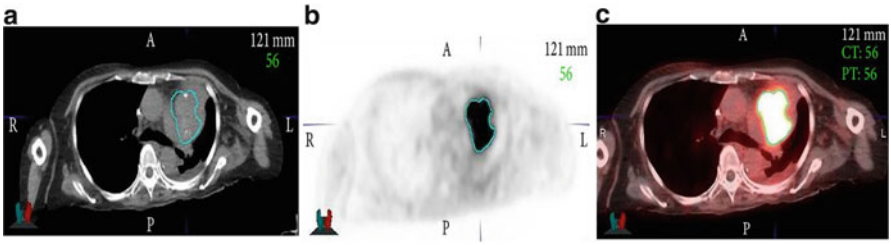

Fig. 5.1 PET images differentiate neoplastic areas with hypermetabolic activity from within the surrounding normal tissue. (**a**) CT image, (**b**) PET image, and (**c**) fused PET/CT image. The teal color marks the gross tumor volume (GTV) as determined from PET image. *Modified and adapted with permission* [18]

MRI

In modern times, magnetic resonance imaging (MRI) has become a highly versatile imaging and diagnostic tool [20]. The technique was developed in the early 1970s and led to a Nobel Prize in Physiology and Medicine to Paul Lauterbur and Peter Mansfield in 2003. MRI involves the detection of nuclear spin reorientation in an applied magnetic field [21]. Compared to CT imaging, MRI has several advantages, such as high temporal and spatial resolution, excellent tissue contrast and tissue penetration, no ionizing radiation, capability of serial studies, and simultaneous acquisition of anatomical structure and physiological function [22]. The intensity of the MR image depends mainly on four parameters: nuclear density; two relaxation times, called T1 (T1 relaxation time is a time constant in which the nuclei align in a given magnetic field) and T2 (T2 is the time constant for loss of phase coherence of excited spins); and motion of the nuclei within the region of interest (ROI). As the nuclear density increases, increasing numbers of nuclei align with the magnetic field, producing a proportionately intense MR signal [21]. Abnormal soft tissue can be better differentiated through measurement of these four parameters compared to any other previous described techniques. MRI-based high soft-tissue contrast allows the assessment of extent and spread of disease, which ultimately can influence radiation treatment volumes [23]. In addition, spatial orientation of the MR image can be performed in any plane, because of the feasibility of manipulating the magnetic field gradients. These inherent advantages of MRI make it a useful imaging method for the evaluation of neurological, musculoskeletal structures, cancer diagnosis, and radiotherapy treatment planning [24–28]. For brain metastases, MRI is much more sensitive than CT, particularly at identifying small lesions ($\leq$0.5 cm) [29]. The ability to visualize tiny lesions prevents patients from aggressive definitive-intent local therapies and allows these lesions to be targeted by stereotactic radiosurgery, which can be delivered with submillimeter accuracy. Additionally, MRI is used for treatment planning in gastrointestinal [30], genitourinary [31, 32], head and neck [33], gynecologic [34], and sarcomatous tumors [23]. By attaching paramagnetic labels to appropriate targeting ligands, MR signal intensity and contrast can be modulated

to directly or indirectly obtain functional information of the labeled target, for example, ^{1}H MRI of tissue water protons can be used to indirectly image membrane receptors, such as ERBB 2 (also known as HER-2) on breast cancer cells [35], the integrin αvβ3 on endothelial cells [36–38], and the phospholipid phosphatidylserine on the surface of apoptotic cells [39, 40]. MR image resolution in vivo at the single cell level is currently not possible; however, it is possible to image the presence of single cells using iron oxide-based nanometer or micrometer-sized particles. The effect of these particles on the surrounding magnetic field extends beyond the boundaries of the cell enabling imaging of single cell [41]. This technique has been used to track implanted stem cells in the brain and spinal cord [42, 43], to monitor T-cell trafficking in immunogenic tumors [44, 45], and to image the location of implanted dendritic cells in the clinic [46].

Imaging of Tumor Metabolism

In recent years, molecular imaging of tumor metabolism has gained considerable interest. Several preclinical studies have indicated relationship between activation of various oncogenes and alterations in cellular metabolism, now considered as one of the hallmarks of cancer [47, 48]. In normal mammalian cells under aerobic conditions, mitochondria oxidize pyruvate to CO_2 and H_2O while generating energy equivalents. Conversion of glucose to lactic acid even in the presence of oxygen is termed as aerobic glycolysis and frequently noticed in malignant cells. Otto Warburg first reported this phenomenon at the beginning of the twentieth century as a specific metabolic abnormality of cancer cells, commonly known as "Warburg effect." He hypothesized that cancer arises from a defect in mitochondrial metabolism leading to aerobic glycolysis [49]. Over time studies conducted in human and rodent glioma cells exhibited high or moderate susceptibility to inhibitors of oxidative phosphorylation, and glioma cells exhibiting high glycolytic phenotype oxidized pyruvate and glutamine even when glucose levels were found to be low [50]. These experimental data suggested that a mitochondrial defect is not a prerequisite for the genesis of cancer and in a strict sense disproved Warburg's hypothesis. Nevertheless, several studies have confirmed frequent overexpression of glucose transporters and glycolytic enzymes in malignant tumors including brain, head and neck, breast, and prostate cancer indicating altered glucose metabolism [51, 52].

^{18}F-FDG PET/CT

^{18}F-fluorodeoxyglucose (FDG) is the most commonly used and the only oncologic PET tracer approved by the Food and Drug Administration (FDA) for routine clinical monitoring of tumor glucose metabolism. More than 90% of oncologic PET imaging is performed by FDG-PET due to the increased metabolism of glucose by

most of the solid tumors including the lung, colorectal, esophageal, stomach, head and neck, cervical, ovarian, breast, melanoma, and most types of lymphomas. In addition to diagnosis, staging, restaging, and monitoring response to cancer treatment, FDG-PET can be useful for selection or delineation of radiotherapy target volumes. FDG-PET has been used as a dose-painting target for sub-volume boosting and thus guiding radiotherapy planning. The use of FDG-PET for radiotherapy planning purposes has shown increasing importance, as more and more radiation oncologists believe that target volume selection and delineation can be adequately performed using FDG-PET in certain cancer types such as non-small cell lung carcinoma (NSCLC) stage N2-N3 patients [53]. In head and neck squamous cell carcinoma (HNSCC), methodological studies have shown that the use of pre-radiotherapy using FDG-PET led to a better estimate of the exact tumor volume, as defined by the pathologic specimens, compared with CT and MRI. Interestingly, when validated segmentation tools were used, the mean FDG-PET-based GTV was consistently smaller than the GTV defined from morphologic imaging in all investigated tumor locations and at all-time points during radiotherapy (Fig. 5.2a) [12, 56, 57]. ^{18}F-FDG PET/CT is also increasingly used for monitoring tumor response after completion of therapy as demonstrated for malignant lymphoma lung, colon, and breast cancer [58]. An example from a lymphoma patient shown in Fig. 5.2b demonstrates that high metabolic activity (measured by high uptake of FDG) of the tumor before the therapy had reduced after the therapy (indicated by reduced FDG uptake), indicating the efficacy of the treatment [54]. Persistently increased FDG uptake after treatment is also associated in predicting a high risk for early disease recurrence and poor prognosis. In patients with Hodgkin's disease and aggressive non-Hodgkin's lymphoma, ^{18}F-FDG PET showed very promising results for assessing tumor response early in the course of therapy. This study included 260 patients with Hodgkin's lymphoma and utilized ^{18}F-FDG PET before and after two cycles of chemotherapy to monitor tumor response. The 2-year progression-free survival for patients with positive PET results after two cycles of chemotherapy was 13 %, whereas it was 95 % for patients with a negative PET scan. In a univariate analysis, the treatment outcome was significantly associated with PET response after two cycles of chemotherapy and various well-known clinical prognostic factors such as stage and the international prognostic score (IPS). In multivariate analyses, however, only positive PET results after two cycles of chemotherapy turned out to be significantly correlated with patient survival ($P < 0.0001$). These data indicated that tumor response in ^{18}F-FDG PET after two cycles of chemotherapy is a stronger predictor of patient outcome than the IPS and other well-established clinical prognostic factors [59]. The results from this study concluded that ^{18}F-FDG PET appears to be the single most important tool for risk-adapted treatment in Hodgkin's lymphoma [59]. The ability of ^{18}F-FDG PET to predict tumor response early in the course of therapy as in the case of Hodgkin's lymphoma offers the opportunity to intensify treatment in patients who are unlikely to respond to first-line chemotherapy. Conversely, treatment could be shortened in patients who show a favorable response after two cycles of chemotherapy. This is of particular interest in Hodgkin's lymphoma, since chemotherapy combined with radiotherapy can cure most of the

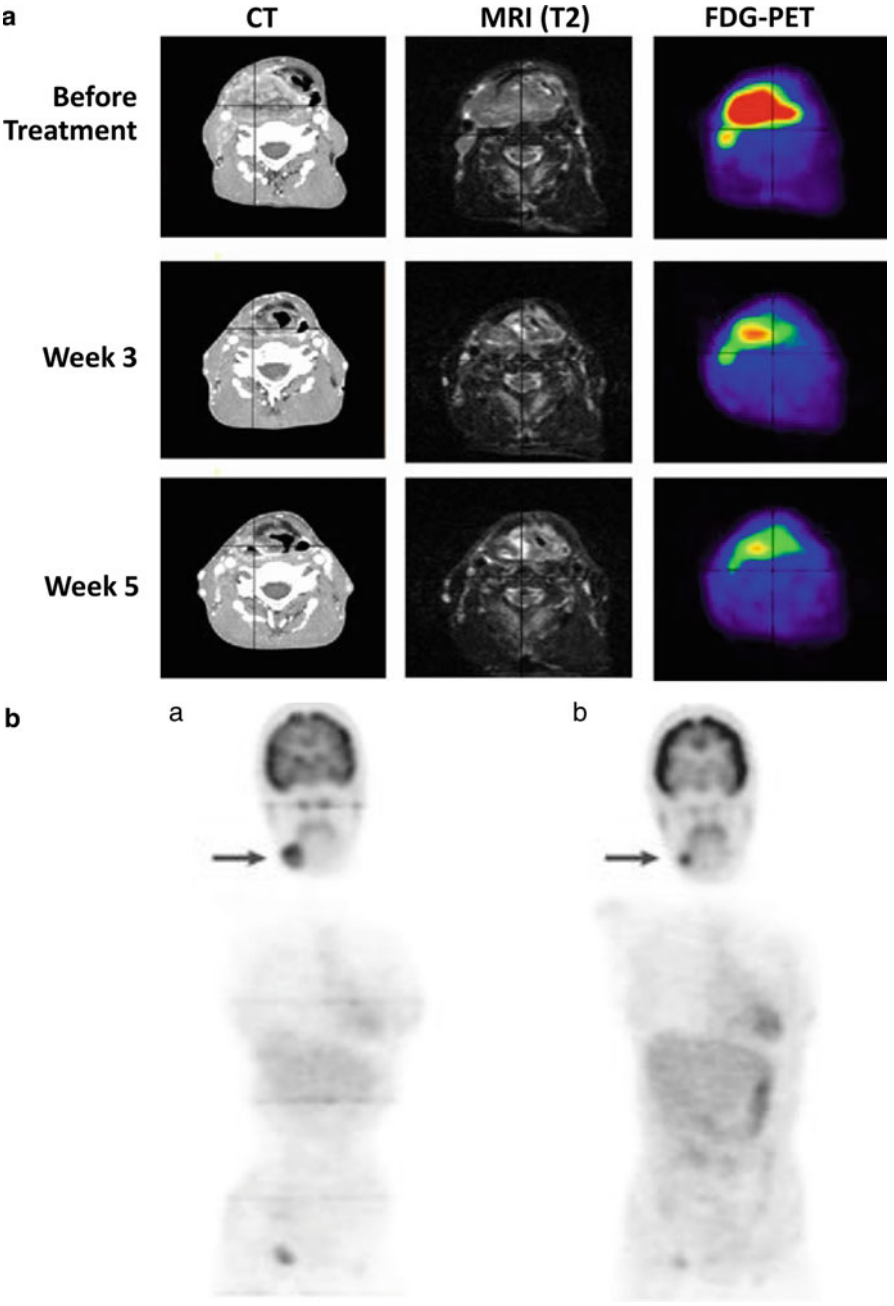

Fig. 5.2 (**a**) An example showing application of FDG-PET over conventional CT and MRI (T2-weighted sequence). A patient with right-sided hypopharyngeal squamous cell carcinoma received concomitant chemoradiotherapy. Images were obtained using intravenous contrast CT, MRI (T2-weighted sequence), and FDG-PET before treatment (*upper panel*) and at the end of weeks 3 and 5 of 30 Gy and 50 Gy radiation dose, respectively (*lower two panels*).

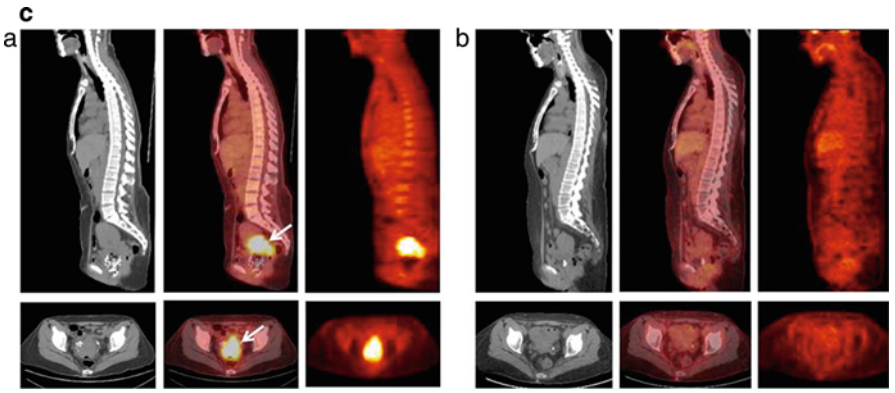

Fig. 5.2 (continued) FDG-PET imaging depicted the most pronounced decrease in tumor volume post therapy compared to CT or MRI. Modified and adapted with permission from [12]. (**b**) FDG-PET-based imaging to determine response to chemotherapy. (*a*) High FDG-PET uptake of 2-[^{18}F] fluoro-2-deoxy-D-glucose (FDG) in a patient with lymphoma arrowed before (*a*) and reduced uptake after (*b*) drug chemotherapy, seen in the tumor and brain. Modified and adapted with permission from [54]. (**c**) Application of ^{18}F-FDG-PET to assess complete metabolic response. PET/CT image of 52-year-old women diagnosed with stage IVA squamous cell cancer of the cervix. (*a*) Sagittal (*top*) and transaxial (*bottom*) CT (*left*), fused PET/CT (*middle*), and PET (*right*) images taken at the initial stage demonstrate high ^{18}F-FDG uptake within the cervical mass. (*b*) Sagittal (*top*) and transaxial (*bottom*) CT image (*left*), fused PET/CT (*middle*) image, and PET (*right*) image taken 3 months after concurrent radiotherapy clearly showing resolution of cervical mass with mild or diffuse uptake of ^{18}F-FDG within the cervix, depicting complete metabolic response. Adapted with permission from [55]

patients but also puts them at increased risk for secondary malignancies and other serious long-term complications, such as infertility and cardiopulmonary toxicity. Focal ^{18}F-FDG uptake after chemo- or radiotherapy has been shown to be a strong prognostic factor. In one of the largest prospective studies published so far, Schwarz et al. [55, 60] prospectively performed ^{18}F-FDG PET in patients with cervical cancer treated by chemoradiotherapy. Post therapy ^{18}F-FDG PET (2–4 months later) showed a complete metabolic response (Fig. 5.2c) in 70 % of the patients, a partial metabolic response in 16 %, and progressive disease in 13 % of patients. The 3-year progression-free survival rates of these patient subgroups were estimated to be 78 %, 33 %, and 0 %, respectively ($P < 0.001$) [55, 60]. Another application of ^{18}F-FDG PET could be in deciding sub-volumes within tumor or lymph nodes that demonstrate high metabolic activity and therefore represent high-risk lesions to be selectively treated with an increased radiation dose. Several studies in rectal and lung cancer have shown that FDG-PET allows selective boosting of hypermetabolic areas. For example, in a study conducted in patients with small-cell lung cancer, FDG-PET-based radiation planning for mediastinal lymph nodes changed the radiotherapy field in 24 % of the patients [61]. In patients with head and neck cancer, the radiation boost dose was markedly elevated and directed at the tumors with the highest FDG-avidity, and the adverse treatment-related effects remained limited [62].

Despite its great clinical utility, FDG-PET has a few limitations. The technique has lower sensitivity for slow growing, metabolically less active tumors (such as prostate, thyroid, and neuroendocrine tumors), and high levels of uptake in some normal tissues, such as the brain, that can make quantification of tumor uptake specifically difficult. Accumulation of PET tracers in infiltrating inflammatory cells, which also show high glycolysis, might give false-positive results and limit the sensitivity of the technique for detecting tumor response to treatment [63].

Hyperpolarized Metabolic MR

Hyperpolarized ^{13}C MRI is an emerging molecular imaging technique that can provide unprecedented gain in amplifying signal intensity. This technique can be used to monitor uptake and metabolism of ^{13}C-labeled endogenous biomolecules such as glucose, pyruvate, fumarate, etc. [64, 65]. The degree and magnitude of the increase in sensitivity of biomolecules depend on the extent of polarization achieved, the T1 relaxation time of the agent, the delivery time, and the MR imaging methods employed. The polarization of ^{13}C at a magnetic field strength of 3 T is calculated to be 2.5 ppm. Consequently, biological molecules enriched with ^{13}C suffer from poor sensitivity because of a lower magnetic moment, lower polarization, and reduced concentrations compared to tissue water proton (in range of a few mM versus 80 M for water ^{1}H). As a result of these differences, ~ four orders of sensitivity difference for ^{13}C-containing molecules compared to water protons need to be bridged to implement metabolic imaging using endogenous organic molecules. Increasing the polarization (fraction of molecules with nuclear spins emitting signal) needs to be increased significantly. Among the various methods used to enhance the polarization of nuclei, dynamic nuclear polarization (DNP) technique has so far been the most successful for in vivo applications [64–66]. In DNP, the higher polarization of a molecule with an unpaired electron spin is transferred to nuclei such as ^{1}H, ^{13}C, ^{15}N and ^{19}F, etc. Firstly, for a molecule to be sufficiently polarized with long signal decay, it should possess a carbon site with long intrinsic T1 that can be enriched in ^{13}C (e.g., carbonyl or carboxylic acid). Introducing deuterium in aliphatic carbons has been shown to be very amenable. Secondly, the molecule should be able to form a homogenous glassy solid formulation with the paramagnetic agent as when frozen it must ensure polarization transfer from the electrons to nuclei. Thirdly, upon dissolution the loss of polarization should be marginal and not significantly high. Fourthly, the chemical shifts of the injected molecule and products should be clearly distinct. Lastly, the molecule should not exhibit any associated side effects when injected as a bolus at the required doses (typically approx. 0.1 mmol/kg body weight). Pyruvate labeled with ^{13}C in the C-1 position satisfies all the prerequisite conditions listed above for a polarized agent. Hyperpolarization of pyruvate is achieved by mixing ^{13}C-labeled compounds with an electron paramagnetic agent (EPA), e.g., OXO-63. The mixed entity is then placed in a 3.35-T magnetic field, cooled to ~1 K, and microwaves are used to transfer polarization from the electron

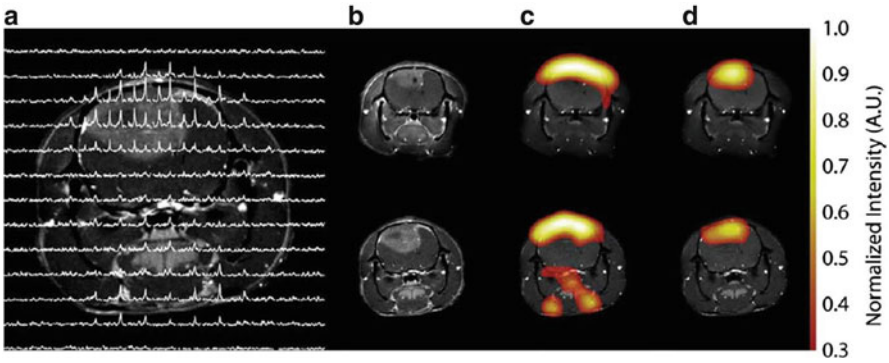

Fig. 5.3 Representative images of hyperpolarized ^{13}C pyruvate (**c**) and lactate (**d**) in a C6 glioma-bearing animal before (*top*) and 96 h after radiotherapy (*bottom*). ACSI dataset is shown in (**a**). The chemical shift images were superimposed on grayscale T1-weighted proton images (**b**) for anatomical reference. The lactate signals, in the false color images, were normalized to the maximum pyruvate signal in each dataset. The lactate signal was reduced following exposure to 15-Gy radiation [67]. *CSI* chemical shift imaging

spin of the EPA to the ^{13}C nuclei of the biomolecule [66]. Once the polarization is achieved, the sample is rapidly dissolved with hot, sterile water and neutralized to physiological pH, temperature, and osmolality. Hyperpolarized ^{13}C pyruvate can be intravenously injected where it metabolized in tissues to various metabolites such as bicarbonate, lactate, and alanine depending on the dominant metabolic pathway in the tissue of interest in vivo. The conversion of pyruvate to each of these metabolites can be imaged using chemical shift MRI or MR spectroscopic imaging (MRSI). The data acquisition utilizing hyperpolarized pyruvate is very rapid, approximately 60 s for [1-^{13}C] pyruvate at 3 T. Several studies have shown the preclinical application of using hyperpolarized pyruvate [64, 65]. Studies examined hyperpolarized ^{13}C pyruvate and lactate in a C6 glioma-bearing animal before radiotherapy (Fig. 5.3b–d, top) and 96 h after radiotherapy (Fig. 5.3b–d, bottom). Comparison of spectra from tumor voxels with those on the contralateral side of the brain indicated high lactate signal in the tumor than in the brain (Fig. 5.3a). ^{13}C chemical shift images acquired following intravenous injection of hyperpolarized [1-^{13}C] pyruvate into rats with implanted C6 gliomas showed significant labeling of lactate within the tumors but comparatively low levels in the surrounding brain. Labeled pyruvate signal was observed at high levels in blood vessels above the brain and from other major vessels elsewhere but was detected at only low levels in the tumor and in the brain [67, 68]. The ratio of hyperpolarized ^{13}C label in tumor lactate compared with the maximum pyruvate signal in the blood vessels was decreased from 0.38 to 0.23 (a reduction of 34 %) by 72 h following whole-brain irradiation with 15 Gy (Fig. 5.3) [67]. Further studies in a transgenic adenocarcinoma of the mouse prostate (TRAMP) model demonstrated elevated levels of hyperpolarized [1-^{13}C] lactate in tumor, with the ratio of [1-^{13}C] lactate/[1-^{13}C] pyruvate being increased in high-grade tumors and decreased after successful treatment (Fig. 5.4) [69]. The preclinical studies using

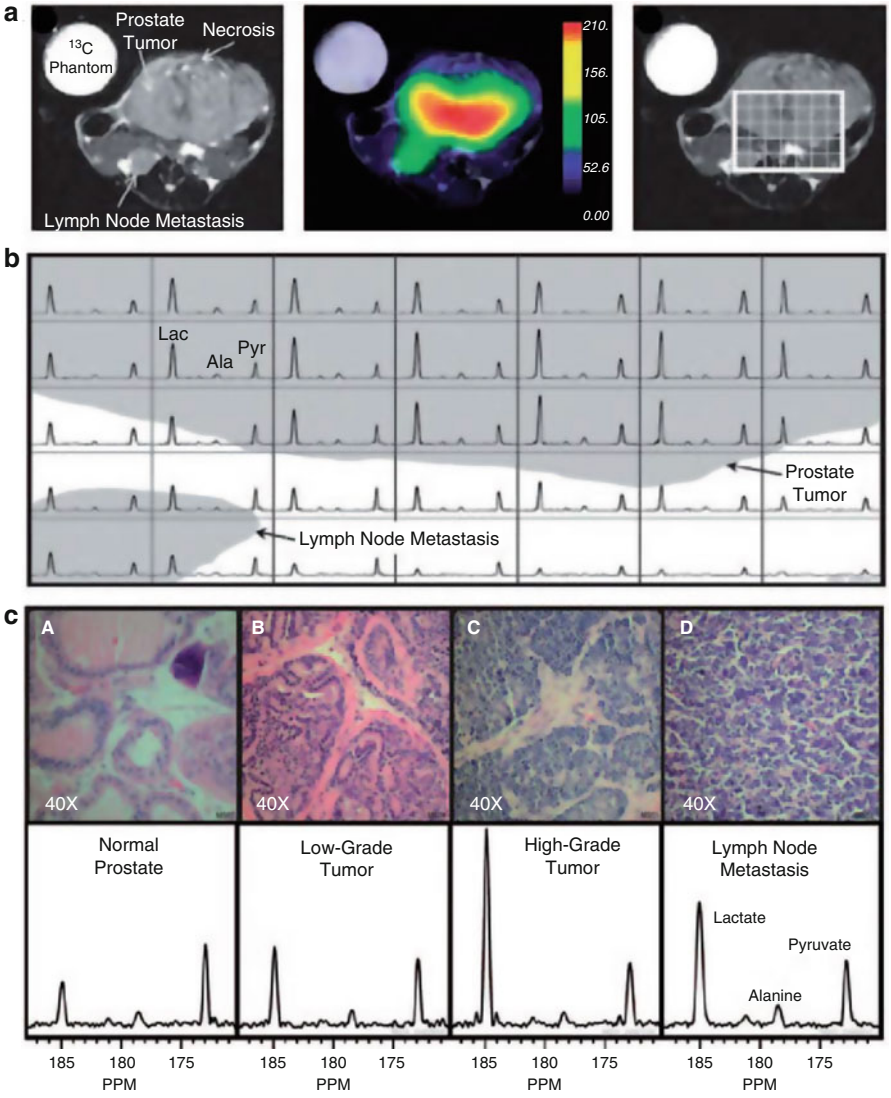

Fig. 5.4 Hyperpolarized ^{13}C metabolic images of a TRAMP mouse. *Upper*: representative anatomical image (**a**) and hyperpolarized ^{13}C lactate image (**b**) following the injection of hyperpolarized [1-^{13}C] pyruvate, overlaid on T2-weighted ^{1}H image. *Middle*: hyperpolarized ^{13}C spectra of primary prostrate and metastatic tumor regions. (**c**) *Lower*: 3D MRSI depicting markedly elevated lactate in the high-grade primary tumor compared with the low-grade tumor. This study demonstrated application of hyperpolarized MRSI imaging of lactate-pyruvate ratio as a biomarker for the assessment of radiation therapy response [67]. *Ala* alanine, *Lac* lactate, *Pyr* pyruvate

hyperpolarization of pyruvate has now advanced to human clinical trials. The first human translation of hyperpolarized technology was successfully demonstrated in patients with prostate tumor [70]. In brief, the study imaged 31 untreated patients diagnosed with localized prostate cancer, where 23 patients had Gleason score of 6, 6 patients with Gleason score 7, and 2 patients with Gleason score 8. The initial phase 1 of the study evaluated the safety, feasibility, and tolerability of injected hyperpolarized [1-^{13}C] pyruvate. The study indicated no dose-limiting toxicities associated with hyperpolarized [1-^{13}C] pyruvate. In addition, the median time taken for the dissolution of the agent to delivery into patient was 66 s. The ^{1}D dynamic MRSI data obtained showed higher [1-^{13}C] lactate signal coming from tumor, and no detectable [1-^{13}C] lactate signal came from the area which did not had tumor. The study confirmed correlation between the high lactate signals with prostate cancer grade. In conclusion, the study successfully demonstrated safety, tolerability, kinetics of hyperpolarized pyruvate delivery, and imaging hyperpolarized ^{13}C metabolism (Fig. 5.5). In the future, more studies will be designed utilizing hyperpolarized [1-^{13}C] pyruvate in larger cohorts of patients with different tumor types to firmly acknowledge the correlation with tumor grade and changes with therapy.

Imaging Cellular Proliferation

Measures of tumor cell proliferation can help to assess the degree of tumor aggressiveness. Several in vitro biomarkers and assays have been developed to estimate tumor proliferation correlating its aggressiveness and stage. However, conventional anatomic pathology is limited in its ability to quantify the rate of cellular proliferation and requires invasive biopsies making it difficult to obtain over time from different metastatic lesions of the patient. Therefore, efforts have been taken to develop imaging modalities to noninvasively measure and quantify the rate of cell proliferation. Noninvasive imaging to estimate the rate of tumor cell proliferation has focused on the application of PET in conjunction with tracers for the thymidine salvage pathway of DNA synthesis. A tracer of thymidine has great implications, as it is the only pyrimidine or purine base unique to DNA, thereby measuring only the DNA synthesis. In the clinics, 3-deoxy-3-[^{18}F]fluorothymidine (FLT) is the most widely used PET tracer to noninvasively measure tumor proliferation. The principles and application of FLT/PET imaging-based radiotherapy planning and tumor response are covered comprehensively in the section on clinical imaging and radiotherapy (see Chap. 9). Here we discuss application of spectroscopy-based imaging involving magnetic resonance spectroscopy imaging (MRSI) to measure cellular proliferation and its application in radiotherapy.

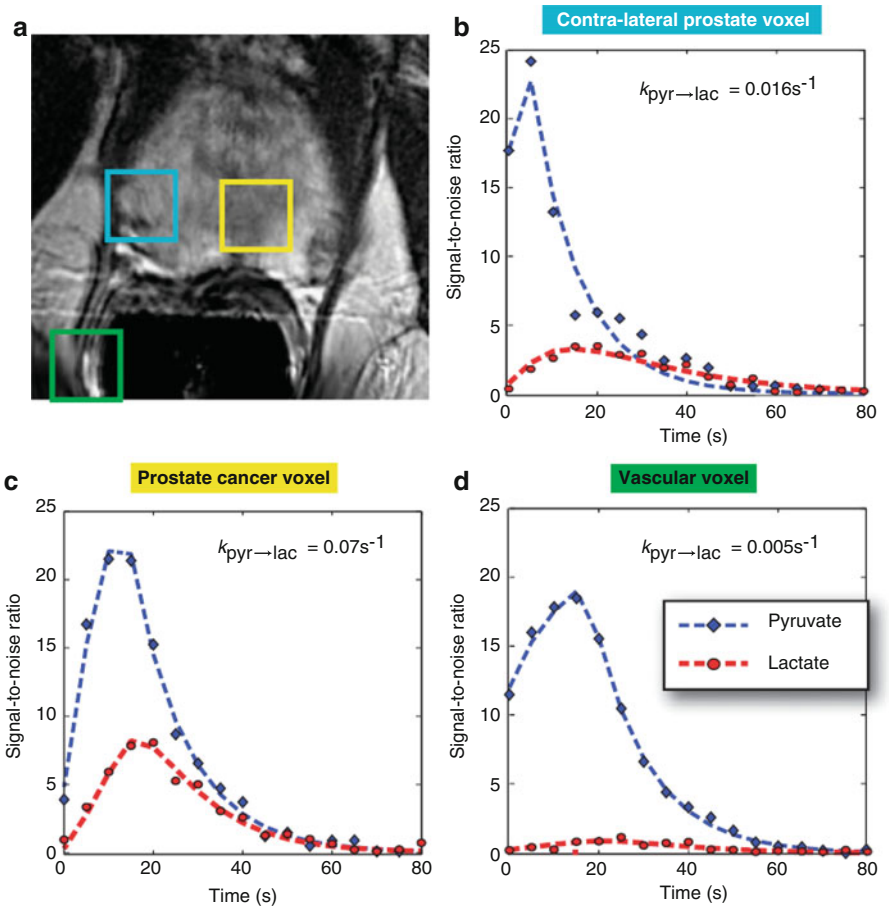

Fig. 5.5 Representative image showing 2D ^{13}C dynamic MRSI data. Images are from a representative patient with a current PSA of 3.6 ng/ml, who had biopsy-proven prostate cancer in the left apex (Gleason grade 3+4) and received the highest dose of hyperpolarized [1-^{13}C] pyruvate (0.43 ml/kg). (**a**) A focus of mild hypo-intensity can be seen on the T2-weighted image, which was consistent with the biopsy findings. (**b**–**d**) 2D localized dynamic hyperpolarized [1-^{13}C] pyruvate and [1-^{13}C] lactate from spectral data that were acquired every 5 s from voxels overlapping the contralateral region of the prostate (*turquoise*), a region of prostate cancer (*yellow*), and a vessel outside the prostate (*green*). The dynamic data were fit as described previously [71]. Data taken with permission from [70]

MRSI

MRSI combines the ability of spectroscopy to acquire a large volume of metabolic information, with the ability of imaging to localize information spatially. Although phosphorus (^{31}P) and carbon (^{13}C) MRSI are possible, proton (^{1}H) MRSI is the technique most often used in clinical settings. On ^{1}H MRSI, tumor spectra contain

resonances from metabolites such as taurine, total choline (choline, phosphocholine, and glycerophosphocholine), total creatine (phosphocreatine and creatine), pyruvate, and lactate.

Among the hallmarks of cancer described by Hanahan and Weinberg, elevated choline metabolism resulting in the accumulation of choline containing compounds such as choline, phosphocholine, and glycerophosphocholine (together represented as tCho) is recognized as an important hallmark, which is amenable for in vivo detection, by MRSI. Studies have shown that malignant transformation rather than just rapid proliferation as the reason for the increased accumulation of tCho is making this a very specific MRI-based imaging biomarker for proliferation [72, 73]. Tumor microenvironmental features such as hypoxia and acidotic extracellular conditions have also been associated with elevated tCho [74]. Several clinical studies already support the strength of monitoring tCho in detecting malignancies and predicting survival. Numerous multi-institutional clinical studies are examining the utility of MRS to detect tCho to aid in the diagnosis and treatment response monitoring.

Imaging Tumor Microenvironment

Tumors survive obtaining oxygen and nutrients passively up to a size of ~2–3 mm^3. For further growth, they invoke neo-angiogenesis to grow new blood vessel network, commonly known as tumor vasculature. While in normal tissue, the angiogenesis processes are tightly regulated resulting in a physically robust vascular network functioning well to deliver oxygen and nutrients, the tumor vascular network is aberrant and not well organized and functions abnormally resulting in a marked heterogeneity in perfusion. As a consequence, tumors exhibit hypoxia and acidotic environments. These are two common features characterizing the tumor microenvironment. Imaging techniques, which can obtain information pertaining to the tumor microenvironment, such as tumor oxygen status, perfusion, and tumor pH, will be useful in both diagnoses and treatment planning.

Development of hypoxia in the tumor microenvironment is highly dynamic process resulting in alterations in cellular metabolism and proliferation. Typically, focal areas of hypoxia are observed in many solid tumors (mainly in the core of the tumor). Tumors exhibit high proliferation ability, and one of the direct consequences of unregulated cellular growth results in a greater demand of oxygen (as well as other nutrients) for energy metabolism. However, unlike normal cells, tumor cells rapidly adapt to hypoxic microenvironment by slowing their growth rate, inhibiting apoptosis, switching mitochondria respiration to glycolysis, stimulating growth of new vasculature (neo-angiogenesis), and promoting metastatic spread. Several preclinical and clinical studies have shown that hypoxic tumors also have elevated expression of key transcription factors notably hypoxia-inducible factor (HIF) expression [75]. A number of hypoxia-related genes, downstream transcription factors, and signaling molecules are also found to be responsible for

the genomic changes within the tumor. Some of the most commonly associated molecular changes associated with tumor hypoxia include elevated expression of endothelial cytokines such as vascular endothelial growth factor (VEGF) and signaling molecules such as IL-1, tumor necrosis factor alpha (TNF-α), transforming growth factor beta (TGF-β), and loss of p53 expression [76]. Increased glycolysis observed in most hypoxic cells leads to accumulation of lactate in the microenvironment resulting in reduced glycolytic activity and increased acidosis (reduced pH) [77]. These changes arising from hypoxia create an environment conducive for tumor progression and development of metastases as well as therapy-resistant clones [77, 78]. Most chemotherapeutic drugs act by inhibiting tumor growth, but when a tumor becomes hypoxic, cells enter a resting phase in their cell cycle and tend to become refractory to these cytotoxic agents. The hypoxia-induced metastatic phenotype is also a contributing factor for the disappointing success of much acclaimed anti-angiogenic therapy. Ionizing radiation is an alternative and effective strategy for killing proliferating cells because the radiation field is homogenous and the killing effect of radiation is independent of vascular delivery. However, radiobiologists have long recognized negative influence of hypoxia on response to radiation therapy as the cytotoxicity of ionizing radiation depends on the level of intracellular O_2. Gray made this observation over 50 years ago that about a three times higher dose of radiation is required to kill hypoxic cells over well-oxygenated cells. Thus, the presence of tumor hypoxia can compromise the effectiveness of radiation treatment.

Another key characteristic of tumor hypoxia is that it is heterogeneously distributed and its dynamics keeps changing over time and with therapy [79]. The blood supply of a malignant tumor is thought to be suboptimal as its vasculature network is immature, leaky, and randomly distributed making it chaotic. This chaotic microvasculature of tumor tissue leads to two types of hypoxia, which can be defined as either diffusion limited or perfusion limited. The first, also known as chronic hypoxia, is the consequence of proliferating cells exceeding the oxygen capacity of the newly formed vascular network. This is because the newly synthesized microvasculature is often insufficient in providing the normoxic microenvironment in the distant tumor areas resulting in diffusion-limited hypoxia [78]. Tumor cells exposed to acute hypoxia have easier access to the blood circulatory system, as they are thought to be nearer the blood vessels. These tumor cells may therefore have greater perfusion limited hypoxia or acute hypoxia, resulting from the structural and functional abnormalities in the newly formed vasculature with poor or insufficient blood supply. Subsequently, this leads to an unstable blood supply to the core of proliferating tumor cells producing intermittent hypoxia. This form of hypoxia is often characterized by rapidly fluctuating oxygen concentration [78]. The relevance of cycling hypoxia in tumor radiobiology and/or conferring radio resistance has been studied using animal models [80, 81]. There are few studies showing evidence of the existence of cycling hypoxia in human tumors. One such study conducted by Pigott et al. examined blood flow in various superficial human tumors, using implanted laser Doppler flow probe. In around 50% of the lesions examined, fluctuations in the flux of red blood cells were observed to be more than a factor of 1.5 correlative

to cycling hypoxia measured in animal models [82]. Another study conducted by Janssen et al. in head and neck cancer patients detected cycling hypoxia by immunohistochemistry [83]. However, all these indirect approaches to assess cycling hypoxia in human tumors are invasive and could not firmly establish any correlation between the overall oxygenation state of the tumors and the incidence of cycling hypoxia.

Methods for Evaluating Hypoxia

Clearly, the ability to identify and quantify tumor oxygenation status and energy metabolism has far-reaching implications in a wide range of medical settings. Most importantly, a clinically useful assay to measure hypoxia, firstly, must be able to distinguish normoxic regions from the ones that are hypoxic at a level relevant to tumor oxygen partial pressure (pO_2) falling in the range of 5–15 mmHg. The ability to simultaneously image tumor oxygenation and metabolic profile can profoundly guide future therapies involving inclusion of radiosensitizers, hypoxia-directed cytotoxins, oxygen-enhanced gas mixtures such as carbogen (a mixture consisting of 95% oxygen and 5% carbon dioxide) [84], and hypoxia-activated prodrugs. Non-toxic prodrugs that generate active species in hypoxic tissue by selective bioreduction have now reached advanced clinical trials. Such hypoxia prodrugs mainly include tirapazamine [85], PR104 [86], and TH-302 [87]. In the early 1990s, hypoxia measurements were achieved by implanting properly calibrated, oxygen-sensitive electrodes (Eppendorf pO_2 histograph) which directly measured pO_2 in units of mmHg [88]. This technique had several practical disadvantages. It is limited to tumors that the probe can be easily accessed, and its invasive nature can cause tissue damage. However, this approach is still in use in the clinic. Other approaches such as immunohistochemistry of tumor tissue using extrinsic hypoxia-specific biomarker such as pimonidazole and intrinsic hypoxia biomarker such as carbonic anhydrase IX (CAIX), VEGF receptor expression, and glucose transporter 1 (Glut1) are utilized to measure hypoxia [89]. These biomarker signatures show poor prognosis and are correlative to the extent of tumor hypoxia. However, the drawback of this approach is that it requires a biopsy, which is challenging and sometimes is not possible. Serum markers have also been evaluated to measure tumor hypoxia but with less success [90, 91]. Furthermore, sampled biomarkers are not able to evaluate spatial heterogeneity, which is often relevant to overall response and is essential for defining a radiation treatment field. Notably, all the above methods do not provide the longitudinal monitoring of hypoxia as the measurement is restricted to only a smaller sub-volume of a tumor. Noninvasive approaches have been instrumental in allowing serial imaging of hypoxia quantitatively and provide valuable information about cycling nature of hypoxia in both space and time. PET hypoxia imaging is noninvasive and routinely used in clinic. Due to the clinical significance of hypoxia imaging, an increasing number of hypoxia PET tracers are available and are being evaluated in the clinical setting. The first radionuclide detection of hypoxia in

tumors was reported using ^{14}C-misonidazole autoradiography [92]. Subsequently, two main tracer classes have been developed to specifically study hypoxia with PET. These tracers are ^{18}F-labeled 2-nitroimidazole derivatives, such as [^{18}F]-fluoromisonidazole ([^{18}F]-FMISO), [18F]-azomycinarabinoside [^{18}F]-FAZA, [18F]-fluoroerythronitroimidazole [^{18}F]-FETNIM, and Cu-labeled diacetyl-bis (N^4-methylthiosemicarbazone) analogues. Among all these tracers, ^{18}F-FMISO is the lead candidate and most extensively studied 2-nitroimidazole-based radiopharmaceutical PET tracer in the clinics. Clinical application of ^{18}F-FMISO in radiotherapy planning and dose painting of different solid tumors is well described in Chap. 9. Despite its potential clinical application, ^{18}F-FMISO imaging in rectal cancer was shown to be compromised by high nonspecific tracer accumulation in normoxic tissue [93]. Several other techniques to measure tumor hypoxia quantitatively and noninvasively are in preclinical development, namely, Overhauser MRI (OMRI), electron paramagnetic resonance imaging (EPRI), and ^{19}F MRI. Electron paramagnetic resonance (EPR) predominantly measures interstitial hypoxia. We describe here highly promising hypoxia imaging modalities that have gained immense attention in both preclinical and clinical setting.

DCE-MRI

Dynamic contrast-enhanced MRI is a powerful MRI technique to examine tissue perfusion profiles. It involves collecting a series of images rapidly following a bolus intravenous administration of the T1 contrast agents, typically gadolinium complexes. Following the bolus administration, these agents localize in the extravascular-extracellular space and are gradually cleared. The time-intensity features from these rapidly acquired sequences of images allow the determination of the microvasculature of the tumors. DCE-MRI has been applied for over a decade to extract functional information regarding the peripheral vascular system such as blood volume, blood flow, vascular permeability, as well as distribution volume and available interstitial space for the contrast agent. DCE-MRI acquires serial MR images before, during, and after the administration of an intravenous contrast agent such as low molecular weight, gadolinium-based (Gd-DTPA) contrast medium. DCE-MRI has grown with the development of anti-angiogenic and neoadjuvant strategies for treating cancer. Angiogenic inhibitors are known to reduce both the number of vessels (particularly non-functional vessels) and their permeability, which can be quantitatively imaged using DCE-MRI. In cervical cancer, DCE-MRI was shown to measure tumor hypoxia in good correlation to Eppendorf oxygen electrode and was an independent predictor of tumor recurrence and death than clinically accepted prognostic factors (e.g., stage, lymph node status, and histology) [94]. Newbold et al. demonstrated a statistically significant correlation between various dynamic contrast-enhanced MR imaging parameters [95], particularly K^{trans} (which represents the permeability of blood vessels) and pimonidazole staining (an exogenous marker for hypoxia). DCE-MR imaging of head and neck squamous cell carcinoma and rectal cancer also has been used to successfully predict treatment response to

chemoradiation therapy [96, 97]. DCE imaging also offers an exciting opportunity to predict the extent of normal tissue function post radiation. Radiation treatment can lead to vascular damage such as vessel dilation, endothelial cell death and apoptosis, microvessel hemorrhage, and eventually vessel occlusion affecting organs such as the brain, liver, and rectum [98–100]. Risk of damaging the normal tissue thereby hinders increasing the radiation dose for better tumor control or even cure. DCE-MRI can be used for early monitoring of vascular response to radiation treatments and predict the outcome of organ function after therapy, thereby selecting the patient who is resistant to radiation for higher dose, potentially leading to a better chance of tumor local control and better overall therapeutic outcome. DCE-MRI/CT thus offers promise of early assessment of tumor response to radiation therapy, opening a window for adaptively optimizing radiation therapy based upon functional alterations that occur earlier than morphological changes and enhancing radiotherapy therapeutic ratio. Although holding great promise, to date DCE-MRI and CT have yet to qualify to be a surrogate endpoint for radiation therapy assessment or for modifying treatment strategies in any prospective phase III clinical trial for any tumor site.

BOLD-MRI

The primary form of functional MRI that uses the blood-oxygen-level dependent (BOLD) contrast was discovered by Seiji Ogawa. In BOLD-MRI hypoxia imaging, the primary source of contrast in images is contributed by the endogenous, paramagnetic deoxyhemoglobin. This technique relies on the delivery of red blood cells to the tissue of interest to provide information about the tissue oxygenation. When hemoglobin becomes saturated with increasing oxygen concentrations, the iron within the heme subunit changes from a paramagnetic high spin state (under hypoxia) to a diamagnetic low spin state (under normoxia). Hoskin et al. evaluated BOLD-MRI sequences to measure regional hypoxia in normal prostate gland and in 20 prostate cancer patients. They validated the reliability and reproducibility of BOLD-MRI with pimonidazole staining of the excised tissues from the same patients [101]. Recently, clinical and preclinical correlations between BOLD-MRI radiotherapy and chemotherapy treatment response have been established. Tissue oxygenation-level-dependent contrast MRI has been shown to corroborate tumor growth delay after irradiation supplemented with hyperoxic breathing in rat prostate tumors [102]. Another pilot study was conducted using BOLD-MRI approach to evaluate response to neoadjuvant chemotherapy in patients with advanced breast cancer [103]. Significantly, higher BOLD response to oxygen breathing was observed in patients who exhibited complete pathological response. These findings establish the effectiveness of BOLD-MRI as a convenient and noninvasive imaging modality in identification of hypoxic subregions within a tumor and providing predictive capabilities for estimating the therapeutic response. Functional MRI (fMRI) has gained unprecedented applications in mapping neural activity of brain in resting and active state. This technique has dominated brain-mapping research since the

early 1950s as it does not require subjects to undergo injections and surgery, or to ingest substances, or be exposed to radiation, etc. However, more studies in future are required to characterize the clinical utility of BOLD-MRI in mapping tumor hypoxia in various types of solid tumors.

EPRI and OMRI

Overhauser-enhanced MRI (OMRI) is a proton-electron double resonance imaging technique that provides anatomically co-registered quantitative pO_2 maps. It uses the enhanced paramagnetic resonance (EPR) transition of the injected paramagnetic agent to enhance the intensity of the tissue water protons. The enhancement is dependent inversely on the tissue oxygen content allowing the determination of pO_2. Briefly, the object to be imaged is placed in a resonator assembly whose resonance frequency has been tuned to the frequencies of both paramagnetic agent and water ^1H when placed in a magnetic field of ~10 mT. By saturating the electron spin of paramagnetic oxygen-sensitive contrast agent, water protons in tissue become hyperpolarized via dynamic nuclear polarization (DNP). The resultant images reflect both the concentration of the contrast agent and local oxygen concentration. However, limitations with this technique made translation to human studies not possible. However, direct imaging of the paramagnetic agent OXO-63 by EPRI has provided advantages over OMRI allowing improved spatial, temporal resolutions and allow dynamic [104, 105] and longitudinal [106] of tumor oxygenation. In principle, EPR is a noninvasive and quantitative imaging technique to measure the pO_2. It is based on the principle where species with unpaired electron exhibiting paramagnetic properties, for example, transition metal complex and free radicals, can be detected. Notably, oxygen exhibits paramagnetic properties and can influence the relaxation rates of the exogenous paramagnetic agent. EPRI is highly sensitive in the detection of changes in oxygen concentrations [107–110]. However, EPR cannot be used to estimate directly the dissolved molecular oxygen. Instead EPR can determine tumor oximetry repeatedly by measuring average tumor pO_2 with minimal perturbation to the microenvironment [111]. Studies have indicated that multisite EPR oximetry is achieved by applying gradient of magnetic field [107, 112, 113]. This approach can simultaneously measure pO_2 at multiple sites in a given tissue of interest. Generally, to obtain EPR image, an exogenous paramagnetic agent is injected to capture the signal. Therefore, an appropriate EPR tracer/agent must meet the indicated criteria: (1) it must be able to generate simple EPR spectra, (2) should have longer pharmacological half-life than the imaging time, and (3) should not confer by itself any associated toxicity. One such agent for EPRI is triarylmethyl radical, OXO-63, used to study tissue oxygen in live animals. The collision interaction between OXO-63 and O_2 broadens the spectral line of OXO-63 in direct proportion to oxygen concentration, thereby enabling a quantitative measure of tissue pO_2 in vivo [114]. The EPRI pO_2 mapping can be co-registered with the host of related physiologic and metabolic information. In a study from our group, we demonstrated that tumor region with higher pO_2 (22.8 mmHg) contained clearly high

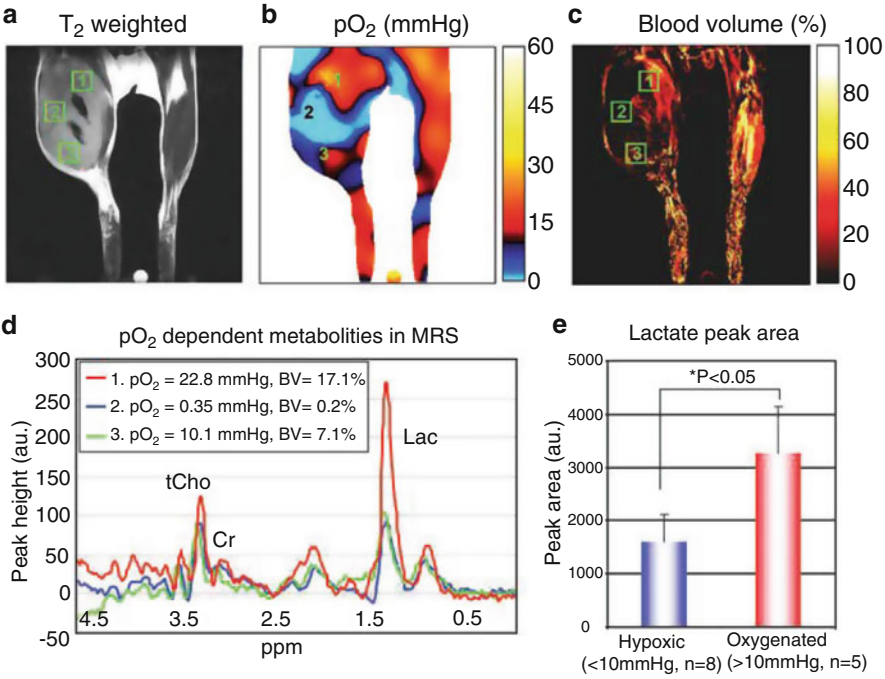

Fig. 5.6 Co-registration of EPRI and MRS/MRI to simultaneously monitor pO_2 distribution and metabolite levels in same tumors. (**a**) T2-weighted anatomical MRI image of SCC tumor-bearing mouse and ROI locations for MRS. (**b**) EPRI pO_2 map of the same animal and the corresponding ROIs chosen for MRS. (**c**) Blood volume image of the slice using USPIO and the corresponding ROIs for MRS. Numbers 1–3 in **a**–**c** correspond with numbers 1–3 in **d**. (**d**) Representative MRS spectra obtained from three different tumor regions selected with different pO_2 and blood volume levels. (**e**) Averaged lactate peak area of MRS spectra obtained from radiobiological hypoxic (<10 mmHg) and normoxic (>10 mmHg) regions. High level of lactate production was detected even in the well-oxygenated tumor region. *BV* blood volume, *MRS* magnetic resonance spectroscopy, *Cr* creatine, *Lac* lactate, *tCho* total choline [111]

levels of lactate (visualized by MRI/MRS) indicating the predominance of aerobic glycolytic process in normoxic tumor regions. In contrary, the averaged lactate peak area observed in radiobiologically oxygenated region (>10 mmHg) was significantly higher than that in hypoxic region (<10 mmHg). The difference in lactate content was attributed to limited blood supply and nutrient supply, as estimated from the blood volume differences in these regions (Fig. 5.6) [111]. With advancement in image formation and reconstitution strategies, it is possible to obtain three-dimensional (3D) maps of pO_2 within 3 min in tumor-bearing mice to enable monitoring of intermittent hypoxia. Studies from our group have shown a successful visualization of dynamic changes of tumor oxygenation over a 30 min time frame using EPRI, where the images were imaged every 3 min, and 3D reconstruction of pO_2, (Fig. 5.7) [67] was achieved. EPRI has also been useful in studying tumor responses to therapy with regard to oxygenation. In another study, changes in

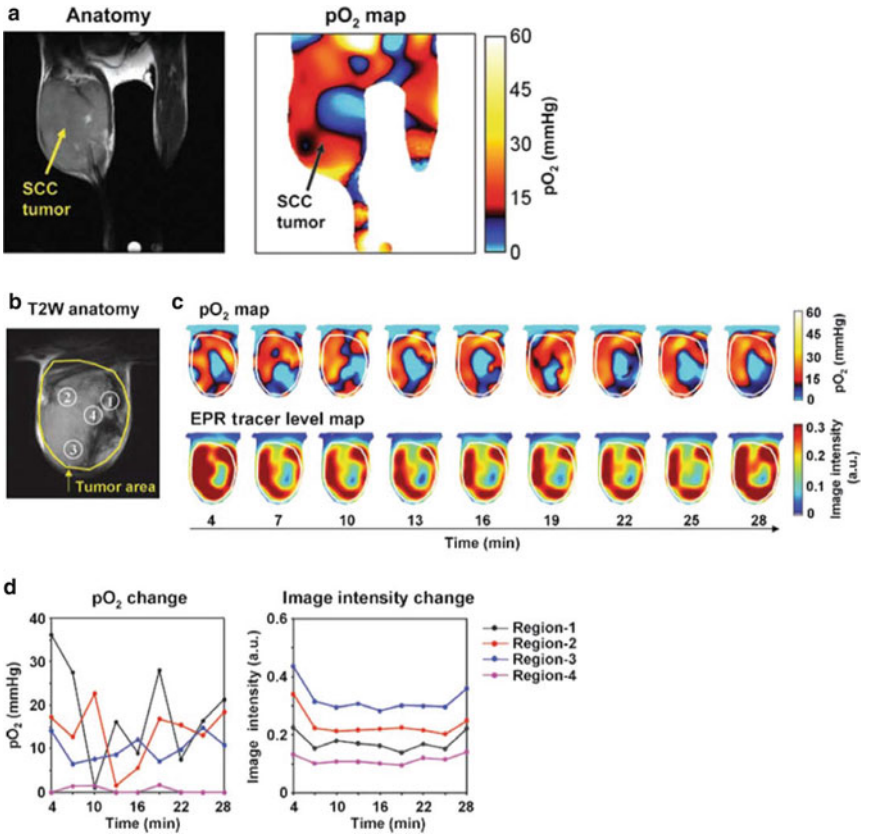

Fig. 5.7 Representative EPRI oxygen image monitoring temporal and spatial dynamics of cycling and chronic hypoxia. (**a**) An EPR oxygen imaging of tumor-bearing mice. The EPRI method allows the pO_2 map from the deep tissue of healthy mouse to be obtained. (**b**) T2-weighted anatomical image of a representative SCCVII tumor-bearing mouse. The large yellow line indicates the tumor region. The four ROIs that are indicated by the small white lines were chosen for tracing fluctuations of pO_2 and spin intensity with time. (**c**) Corresponding pO_2 maps (*top*) and the tracer level maps (*bottom*) were obtained from EPRI. The white line indicates the tumor region. Time increased from *left* to *right* from 4 to 28 min. (**d**) The values of pO_2 and the tracer level in each ROI, described in (b), were quantified and plotted as a function of time. *SCCVII* squamous cell carcinoma VII [67]

chronic and cycling tumor hypoxia were imaged before and 1 day after radiation in an SCCVII murine model (Fig. 5.8). In this study, two regions of cycling and chronic hypoxia were imaged using EPRI. Interestingly, the study indicated that despite no significant changes in tumor volume before or 1 day after radiation, visible changes in cycling and chronic hypoxia were observed. The region of cycling hypoxia showed a decrease, whereas chronic hypoxia regions in the tumor exhibited a significant increase in response to radiation treatment. Matsumoto et al. used EPRI and MRI approaches to demonstrate vascular renormalization in tumor-bearing mice by obtaining longitudinal mapping of tumor pO_2 and microvessel density during

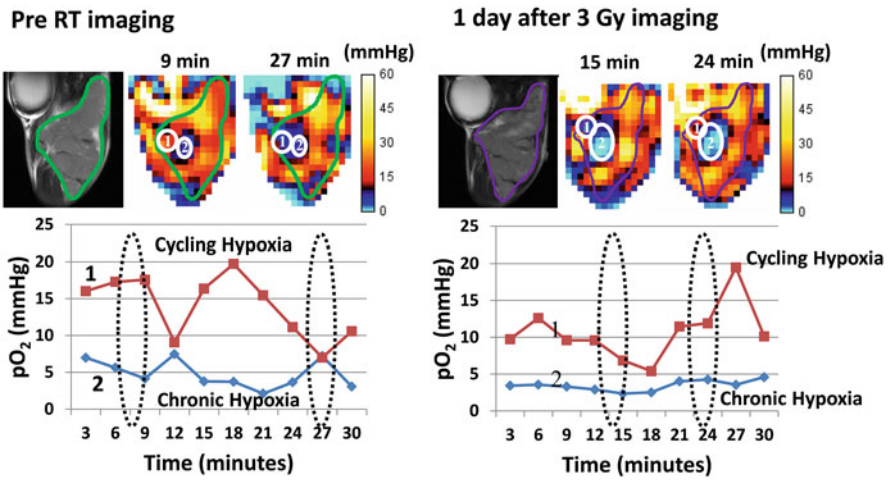

Fig. 5.8 Three-dimensional-EPR oxygen images monitoring the spatial and temporal dynamics of chronic and cycling hypoxia in response to radiation. EPR images obtained from subcutaneous SCCVII tumors in mice before RT and 1 day after irradiation (3 Gy). 1 and 2 marked within white circle represent region of interest (ROI) selected to monitor changes in pO_2 dynamics every 3 min over 30 min time period. ROI 1 represents cycling hypoxia (median $pO_2 > 10$ mmHg during 30 min duration) and ROI 2 represents chronic hypoxia (median $pO_2 < 10$ mmHg during 30 min duration). Representative images and EPR images captured during 9 min and 27 min before RT and at 15 min and 24 min after RT are shown. *EPR* electron paramagnetic resonance, *pO_2* partial pressure of O_2, *ROI* region of interest (Personal communication to Murali C. Krishna)

treatment with the multi-tyrosine inhibitor, sunitinib (Fig. 5.9). This study demonstrated that radiation treatment during the period of improved oxygenation by anti-angiogenic therapy resulted in a synergistic delay in tumor growth. Most importantly, sunitinib treatment suppressed cycling tumor hypoxia [106]. These preclinical results demonstrate a potential of noninvasive monitoring of tumor pO_2 enabling identification of a window of vascular renormalization to maximize the effects of radiation in combination therapy such as anti-angiogenic drugs. Subsequently noninvasive imaging modality can be useful in uncovering the dynamics of functional heterogeneity such as tumor pO_2 associated during and after the response to therapy. Despite its great clinical potential, EPRI is currently available only for preclinical applications. Efforts from radiation biologists, radiation oncologists, and imaging experts are needed to conduct studies toward designing clinical trials and strengthening the application of EPRI, fostering the advancements of this technology for clinical use.

Conclusion

The ultimate aim of molecular and functional imaging approaches in clinical oncology is to improvise cancer diagnosis and treatment. These imaging approaches aid clinicians to visualize tumors and their response to treatments. Research focused on

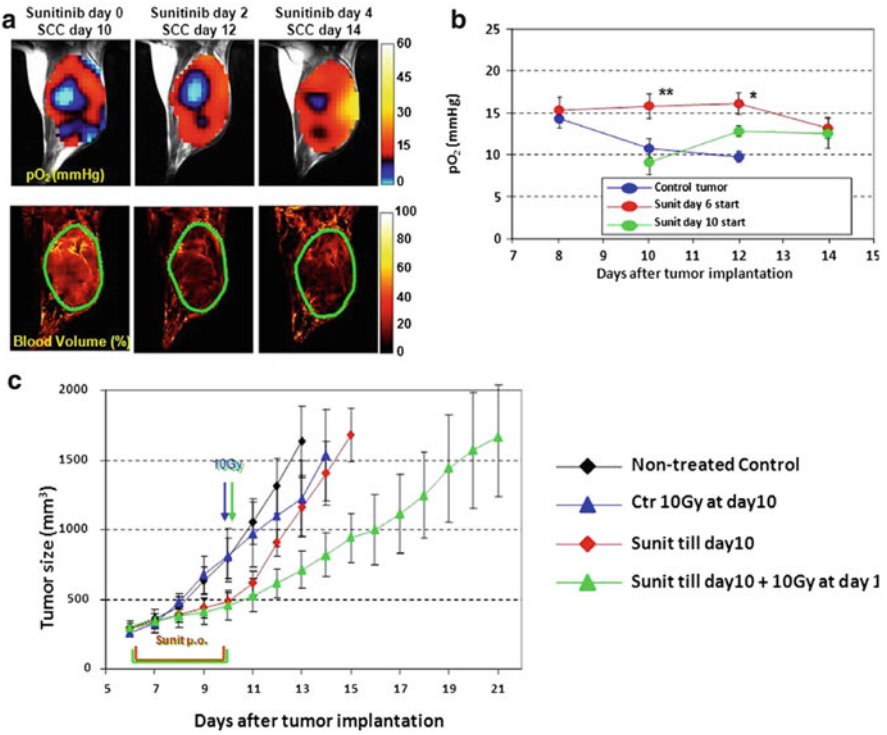

Fig. 5.9 EPRI imaging of tumor pO_2 and blood volume for monitoring chemoradiation response. (**a**) Administration of anti-angiogenic agent sunitinib treatment at later stage of tumor development improved tumor oxygenation (*upper panel*) and reduced tumor blood volume (*lower panel*) without significant change in tumor size. (**b**) Quantification of tumor pO_2 changes in sunitinib-treated mice and vehicle control mice. $^*P<0.05$, $^*P<0.01$. (**c**) Transient increase in tumor oxygenation with sunitinib treatment enhances outcome of radiation therapy. The tumor growth kinetic shown for untreated control mice (*black*), mice treated with a single10-Gy radiation at SCC day 10 (*blue*), mice treated for 4 days with sunitinib during 6–10 days after SCC implantation (*red*), and mice treated for 4 days with sunitinib followed by a single 10 Gy radiation (*green*). *SCC* squamous cell carcinoma. Data taken from [106]

cancer molecular genetics and epigenetics has contributed a number of targeted therapies, whose clinical utility can be successfully characterized using molecular imaging. Future discoveries identifying novel imaging biomarkers will accelerate and improve drug development by helping to determine if the drug under investigation is hitting the desired target and causing the intended effect to tumors. Molecular imaging-based targeted therapy has great potential in making personalized medicine a reality. Collectively, image-guided targeted therapies are the only noninvasive approach that provides real-time intervention rather than facing endpoint failures in cancer management. So far two major tumor characteristics have been well exploited using molecular imaging approaches. These include the altered tumor metabolism and changes in tumor microenvironment such as hypoxia.

Tumor glucose metabolism has been highly successful in monitoring, staging, and early assessment of targeted therapies including radiotherapy in the clinics. The utility of ^{18}F-FDG with PET and MRSI will remain the cornerstone of imaging metabolism in the near future. More advancement in better PET tracers along with our current understanding of altered tumor metabolism and key factors influencing tumor microenvironment will impact future management of cancer patient diagnosis, tumor staging, radiation treatment planning, and monitoring of tumor response to therapy. Tumor hypoxia is another well-characterized biological phenomenon that is prevalent in various solid tumors. Hypoxic tumors tend to be more resistant to radiation-induced death. Years of research have shed light on the cyclic and chronic hypoxia present in solid tumors which is heterogeneously dispersed and is independent of size, stage, grade, or histology of any given tumor. Therefore, noninvasive measurement of tumor hypoxia is of paramount importance in clinical management with radiotherapy. It has been observed that tumors can overcome hypoxia by several different survival mechanisms, including loss of apoptotic potential, increased proliferative potential, and formation of new blood vessels that encourage the evolutionary selection for a more malignant phenotype. Noninvasive techniques such as DCE-MRI and BOLD-MRI have shown some promise in measuring hypoxia noninvasively. Currently, EPRI seems to the highly sensitive technique to measure hypoxia quantitatively. Still, in its infancy, future work needs to be done to make this technique applicable in a clinical setting. Incorporating EPRI/MRSI in radiotherapy will help advance its application in targeting deep-seated, surgically unresolved tumors. The assessment of tumor hypoxia by noninvasive means will be of immense value to radiation oncologists, medical oncologists, and pharmaceutical companies to develop and test hypoxia-based therapies or other combinatorial treatment strategies. Multimodality or hybrid imaging will play a major role in the clinical assessment in the near future. This trend has already been set by the replacement of separate PET and CT by hybrid PET/CT technology and will continue with the establishment of integrated MRI/PET. In summary, application of integrated imaging tools for detecting tumor physiology has tremendous potential in oncology and can improve the effectiveness of radiation therapy.

Future Perspective

A number of promising molecular imaging platforms are emerging to provide radiation oncologists with biochemical and physiological information of tumor and normal tissues before, during, and after treatment. This information has the potential to aid clinicians in diagnosis and perhaps rapid assessment of treatment response. With respect to tumor metabolism, FDG has been and will continue to be useful in diagnosis and monitoring treatment responses. Future, emerging multimodalities for metabolic imaging using hyperpolarized biochemical substrates such as *hyper-PET* may provide better specificity of metabolic processes. This technique utilizes simultaneous in vivo PET combined with hyperpolarized MRI. The first example

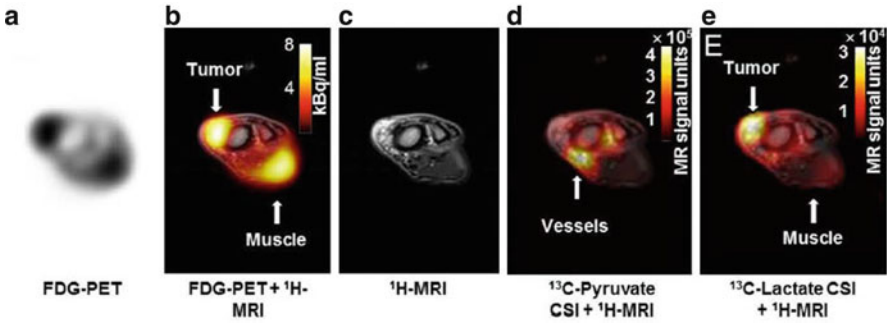

Fig. 5.10 *Hyper-PET* showing sensitivity of ^{13}C-hyperpolarized pyruvate over ^{18}F-FDG to measure tumor glucose metabolism. Image showing right front leg of canine patient with liposarcoma. High uptake of ^{18}F-FDG in muscle (marked in *arrow*, panel **b**, ^{18}F-FDG-PET + ^{1}H-MRI) and of ^{13}C pyruvate in the large vessels (marked in *arrow*, panel **d**, ^{13}C-Pyruvate CSI + ^{1}H-MRI). (**a**) ^{18}F-FDG-PET. (**b**) ^{18}F-FDG-PET + ^{1}H-MRI. (**c**) ^{1}H-MRI. (**d**) ^{13}C-pyruvate CSI + ^{1}H-MRI. (**e**) ^{13}C-lactate CSI + ^{1}H-MRI. Data taken with permission from [115]

demonstrating the application of *hyper-PET* has recently been tested in canine liposarcoma model [115]. In this study, ^{13}C-hyperpolarized pyruvate was combined with ^{18}F-FDG-PET and MRI to assess the feasibility and specificity of glucose uptake by tumor over normal muscle tissue. Interestingly, the muscle forepaw of the subject indicated significantly high ^{18}F-FDG uptake compared to ^{13}C-hyperpolarized pyruvate. High ^{18}F-FDG in the normal muscle tissue was attributed to high activity of these muscles before anesthesia. However, real-time conversion of ^{13}C-pyruvate into ^{13}C-lactate corresponding to high ^{18}F-FDG was observed in the tumor tissue (Fig. 5.10). This study confirms the sensitivity and specificity of ^{13}C-hyperpolarized pyruvate for the diagnosis of cancer. Such cross comparison and application of emerging imaging platforms will be necessary to choose and optimize the most accurate functional imaging approach. Lastly, imaging with specific hyperpolarized biochemical substrates may be useful in delineating tumors with specific mutations in metabolic pathways.

The ongoing identification of a variety of tumor specific markers that can be incorporated into imaging platforms will further enhance the clinician's ability to diagnose and monitor treatment response. Imaging that reports on physiological and microenvironmental processes such as diffusion, perfusion, proliferation, and hypoxia, which are known to be important in tumor growth and treatment response, will further enhance the information base. There will also be a need to evaluate many of the new imaging modalities not only for tumor but also for normal tissues within the radiation field. Establishing a therapeutic ratio of radiation and/or chemo-radiation cancer treatment is not always straightforward. It is anticipated that the newer molecular imaging approaches will complement and perhaps hybridize with existing imaging platforms to yield more information, particularly at the biochemical/molecular level that might be used to more precisely derive a therapeutic ratio for various treatment strategies.

References

1. Bedard PL, Hansen AR, Ratain MJ, Siu LL (2013) Tumour heterogeneity in the clinic. Nature 501:355–364
2. Junttila MR, de Sauvage FJ (2013) Influence of tumour micro-environment heterogeneity on therapeutic response. Nature 501:346–354
3. Cardenas-Navia LI, Mace D, Richardson RA, Wilson DF, Shan S, Dewhirst MW (2008) The pervasive presence of fluctuating oxygenation in tumors. Cancer Res 68:5812–5819
4. Schroeder T, Yuan H, Viglianti BL, Peltz C, Asopa S, Vujaskovic Z, Dewhirst MW (2005) Spatial heterogeneity and oxygen dependence of glucose consumption in R3230Ac and fibrosarcomas of the Fischer 344 rat. Cancer Res 65:5163–5171
5. Serganova I, Doubrovin M, Vider J, Ponomarev V, Soghomonyan S, Beresten T, Ageyeva L, Serganov A, Cai S, Balatoni J, Blasberg R, Gelovani J (2004) Molecular imaging of temporal dynamics and spatial heterogeneity of hypoxia-inducible factor-1 signal transduction activity in tumors in living mice. Cancer Res 64:6101–6108
6. Eskey CJ, Koretsky AP, Domach MM, Jain RK (1992) 2H-nuclear magnetic resonance imaging of tumor blood flow: spatial and temporal heterogeneity in a tissue-isolated mammary adenocarcinoma. Cancer Res 52:6010–6019
7. Hamberg LM, Kristjansen PE, Hunter GJ, Wolf GL, Jain RK (1994) Spatial heterogeneity in tumor perfusion measured with functional computed tomography at 0.05 microliter resolution. Cancer Res 54:6032–6036
8. Degani H, Gusis V, Weinstein D, Fields S, Strano S (1997) Mapping pathophysiological features of breast tumors by MRI at high spatial resolution. Nat Med 3:780–782
9. Choi YP, Shim HS, Gao MQ, Kang S, Cho NH (2011) Molecular portraits of intratumoral heterogeneity in human ovarian cancer. Cancer Lett 307:62–71
10. Gatenby RA, Silva AS, Gillies RJ, Frieden BR (2009) Adaptive therapy. Cancer Res 69:4894–4903
11. Ling CC, Humm J, Larson S, Amols H, Fuks Z, Leibel S, Koutcher JA (2000) Towards multidimensional radiotherapy (MD-CRT): biological imaging and biological conformality. Int J Radiat Oncol Biol Phys 47:551–560
12. Bentzen SM, Gregoire V (2011) Molecular imaging-based dose painting: a novel paradigm for radiation therapy prescription. Semin Radiat Oncol 21:101–110
13. Chen ZY, Wang YX, Lin Y, Zhang JS, Yang F, Zhou QL, Liao YY (2014) Advance of molecular imaging technology and targeted imaging agent in imaging and therapy. BioMed Res Int 2014:819324
14. Anderson CJ, Ferdani R (2009) Copper-64 radiopharmaceuticals for PET imaging of cancer: advances in preclinical and clinical research. Cancer Biother Radiopharm 24:379–393
15. Phelps ME (2000) Positron emission tomography provides molecular imaging of biological processes. Proc Natl Acad Sci U S A 97:9226–9233
16. Zhu A, Lee D, Shim H (2011) Metabolic positron emission tomography imaging in cancer detection and therapy response. Semin Oncol 38:55–69
17. Gambhir SS (2002) Molecular imaging of cancer with positron emission tomography. Nat Rev Cancer 2:683–693
18. Pereira GC, Traughber M, Muzic RF Jr (2014) The role of imaging in radiation therapy planning: past, present, and future. BioMed Res Int 2014:231090
19. Hijnen NM, de Vries A, Nicolay K, Grull H (2012) Dual-isotope 111In/177Lu SPECT imaging as a tool in molecular imaging tracer design. Contrast Media Mol Imaging 7:214–222
20. Blamire AM (2008) The technology of MRI–the next 10 years? Br J Radiol 81:601–617
21. Scherzinger AL, Hendee WR (1985) Basic principles of magnetic resonance imaging–an update. West J Med 143:782–792
22. Gore JC, Manning HC, Quarles CC, Waddell KW, Yankeelov TE (2011) Magnetic resonance in the era of molecular imaging of cancer. Magn Reson Imaging 29:587–600

23. Khoo VS (2000) MRI–"magic radiotherapy imaging" for treatment planning? Br J Radiol 73:229–233
24. Anderson SA, Frank JA (2007) MRI of mouse models of neurological disorders. NMR Biomed 20:200–215
25. Kerkhof EM, Balter JM, Vineberg K, Raaymakers BW (2010) Treatment plan adaptation for MRI-guided radiotherapy using solely MRI data: a CT-based simulation study. Phys Med Biol 55:N433–N440
26. Klostergaard J, Parga K, Raptis RG (2010) Current and future applications of magnetic resonance imaging (MRI) to breast and ovarian cancer patient management. P R Health Sci J 29:223–231
27. Lee DJ, Ahmed HU, Moore CM, Emberton M, Ehdaie B (2014) Multiparametric magnetic resonance imaging in the management and diagnosis of prostate cancer: current applications and strategies. Curr Urol Rep 15:390
28. Schulze M, Kotter I, Ernemann U, Fenchel M, Tzaribatchev N, Claussen CD, Horger M (2009) MRI findings in inflammatory muscle diseases and their noninflammatory mimics. AJR Am J Roentgenol 192:1708–1716
29. Akeson P, Larsson EM, Kristoffersen DT, Jonsson E, Holtas S (1995) Brain metastases–comparison of gadodiamide injection-enhanced MR imaging at standard and high dose, contrast-enhanced CT and non-contrast-enhanced MR imaging. Acta Radiol 36:300–306
30. O'Neill BD, Salerno G, Thomas K, Tait DM, Brown G (2009) MR vs CT imaging: low rectal cancer tumour delineation for three-dimensional conformal radiotherapy. Br J Radiol 82:509–513
31. Chen L, Price RA Jr, Wang L, Li J, Qin L, Mcneeley S, Ma CM, Freedman GM, Pollack A (2004) MRI-based treatment planning for radiotherapy: dosimetric verification for prostate IMRT. Int J Radiat Oncol Biol Phys 60:636–647
32. O'Connor JP, Tofts PS, Miles KA, Parkes LM, Thompson G, Jackson A (2011) Dynamic contrast-enhanced imaging techniques: CT and MRI. Br J Radiol 84:S112–S120
33. Newbold K, Partridge M, Cook G, Sohaib SA, Charles-Edwards E, Rhys-Evans P, Harrington K, Nutting C (2006) Advanced imaging applied to radiotherapy planning in head and neck cancer: a clinical review. Br J Radiol 79:554–561
34. Barillot I, Reynaud-Bougnoux A (2006) The use of MRI in planning radiotherapy for gynaecological tumours. Cancer Imaging 6:100–106
35. Artemov D, Mori N, Ravi R, Bhujwalla ZM (2003) Magnetic resonance molecular imaging of the HER-2/neu receptor. Cancer Res 63:2723–2727
36. Debergh I, van Damme N, de Naeyer D, Smeets P, Demetter P, Robert P, Carme S, Pattyn P, Ceelen W (2014) Molecular imaging of tumor-associated angiogenesis using a novel magnetic resonance imaging contrast agent targeting alphavbeta 3 integrin. Ann Surg Oncol 21:2097–2104
37. Schnell O, Krebs B, Carlsen J, Miederer I, Goetz C, Goldbrunner RH, Wester HJ, Haubner R, Popperl G, Holtmannspotter M, Kretzschmar HA, Kessler H, Tonn JC, Schwaiger M, Beer AJ (2009) Imaging of integrin alpha(v)beta(3) expression in patients with malignant glioma by [18F] Galacto-RGD positron emission tomography. Neuro Oncol 11:861–870
38. Sipkins DA, Cheresh DA, Kazemi MR, Nevin LM, Bednarski MD, Li KC (1998) Detection of tumor angiogenesis in vivo by alphaVbeta3-targeted magnetic resonance imaging. Nat Med 4:623–626
39. Blankenberg FG (2008) In vivo imaging of apoptosis. Cancer Biol Ther 7:1525–1532
40. Maiseyeu A, Mihai G, Kampfrath T, Simonetti OP, Sen CK, Roy S, Rajagopalan S, Parthasarathy S (2009) Gadolinium-containing phosphatidylserine liposomes for molecular imaging of atherosclerosis. J Lipid Res 50:2157–2163
41. Dodd SJ, Williams M, Suhan JP, Williams DS, Koretsky AP, Ho C (1999) Detection of single mammalian cells by high-resolution magnetic resonance imaging. Biophys J 76:103–109
42. Bulte JW, Zhang S, van Gelderen P, Herynek V, Jordan EK, Duncan ID, Frank JA (1999) Neurotransplantation of magnetically labeled oligodendrocyte progenitors: magnetic resonance tracking of cell migration and myelination. Proc Natl Acad Sci U S A 96:15256–15261

43. Franklin RJ, Blaschuk KL, Bearchell MC, Prestoz LL, Setzu A, Brindle KM, ffrench-Constant C (1999) Magnetic resonance imaging of transplanted oligodendrocyte precursors in the rat brain. Neuroreport 10:3961–3965
44. Hu DE, Kettunen MI, Brindle KM (2005) Monitoring T-lymphocyte trafficking in tumors undergoing immune rejection. Magn Reson Med 54:1473–1479
45. Kircher MF, Allport JR, Graves EE, Love V, Josephson L, Lichtman AH, Weissleder R (2003) In vivo high resolution three-dimensional imaging of antigen-specific cytotoxic T-lymphocyte trafficking to tumors. Cancer Res 63:6838–6846
46. de Vries IJ, Lesterhuis WJ, Barentsz JO, Verdijk P, van Krieken JH, Boerman OC, Oyen WJ, Bonenkamp JJ, Boezeman JB, Adema GJ, Bulte JW, Scheenen TW, Punt CJ, Heerschap A, Figdor CG (2005) Magnetic resonance tracking of dendritic cells in melanoma patients for monitoring of cellular therapy. Nat Biotechnol 23:1407–1413
47. Dang CV (2012) Links between metabolism and cancer. Genes Dev 26:877–890
48. Hanahan D, Weinberg RA (2011) Hallmarks of cancer: the next generation. Cell 144: 646–674
49. Warburg O (1956) On respiratory impairment in cancer cells. Science 124:269–270
50. Griguer CE, Oliva CR, Gillespie GY (2005) Glucose metabolism heterogeneity in human and mouse malignant glioma cell lines. J Neurooncol 74:123–133
51. Carvalho KC, Cunha IW, Rocha RM, Ayala FR, Cajaiba MM, Begnami MD, Vilela RS, Paiva GR, Andrade RG, Soares FA (2011) GLUT1 expression in malignant tumors and its use as an immunodiagnostic marker. Clinics (Sao Paulo) 66:965–972
52. Macheda ML, Rogers S, Best JD (2005) Molecular and cellular regulation of glucose transporter (GLUT) proteins in cancer. J Cell Physiol 202:654–662
53. van Der Wel A, Nijsten S, Hochstenbag M, Lamers R, Boersma L, Wanders R, Lutgens L, Zimny M, Bentzen SM, Wouters B, Lambin P, De Ruysscher D (2005) Increased therapeutic ratio by 18FDG-PET CT planning in patients with clinical CT stage N2-N3M0 non-small-cell lung cancer: a modeling study. Int J Radiat Oncol Biol Phys 61:649–655
54. Brindle K (2008) New approaches for imaging tumour responses to treatment. Nat Rev Cancer 8:94–107
55. Schwarz JK, Siegel BA, Dehdashti F, Grigsby PW (2007) Association of posttherapy positron emission tomography with tumor response and survival in cervical carcinoma. JAMA 298:2289–2295
56. Daisne JF, Duprez T, Weynand B, Lonneux M, Hamoir M, Reychler H, Gregoire V (2004) Tumor volume in pharyngolaryngeal squamous cell carcinoma: comparison at CT, MR imaging, and FDG PET and validation with surgical specimen. Radiology 233:93–100
57. Geets X, Lee JA, Bol A, Lonneux M, Gregoire V (2007) A gradient-based method for segmenting FDG-PET images: methodology and validation. Eur J Nucl Med Mol Imaging 34:1427–1438
58. Kostakoglu L, Goldsmith SJ (2003) 18F-FDG PET evaluation of the response to therapy for lymphoma and for breast, lung, and colorectal carcinoma. J Nucl Med 44:224–239
59. Gallamini A, Hutchings M, Rigacci L, Specht L, Merli F, Hansen M, Patti C, Loft A, Di Raimondo F, D'amore F, Biggi A, Vitolo U, Stelitano C, Sancetta R, Trentin L, Luminari S, Iannitto E, Viviani S, Pierri I, Levis A (2007) Early interim 2-[18F]fluoro-2-deoxy-D-glucose positron emission tomography is prognostically superior to international prognostic score in advanced-stage Hodgkin's lymphoma: a report from a joint Italian-Danish study. J Clin Oncol 25:3746–3752
60. Schwarz JK, Grigsby PW, Dehdashti F, Delbeke D (2009) The role of 18F-FDG PET in assessing therapy response in cancer of the cervix and ovaries. J Nucl Med 50(Suppl 1): 64S–73S
61. van Loon J, Offermann C, Bosmans G, Wanders R, Dekker A, Borger J, Oellers M, Dingemans AM, van Baardwijk A, Teule J, Snoep G, Hochstenbag M, Houben R, Lambin P, De Ruysscher D (2008) 18FDG-PET based radiation planning of mediastinal lymph nodes in limited disease small cell lung cancer changes radiotherapy fields: a planning study. Radiother Oncol 87:49–54

62. Madani I, Duthoy W, Derie C, De Gersem W, Boterberg T, Saerens M, Jacobs F, Gregoire V, Lonneux M, Vakaet L, Vanderstraeten B, Bauters W, Bonte K, Thierens H, De Neve W (2007) Positron emission tomography-guided, focal-dose escalation using intensity-modulated radiotherapy for head and neck cancer. Int J Radiat Oncol Biol Phys 68:126–135
63. Juweid ME, Cheson BD (2006) Positron-emission tomography and assessment of cancer therapy. N Engl J Med 354:496–507
64. Golman K, Ardenkjaer-Larsen JH, Petersson JS, Mansson S, Leunbach I (2003) Molecular imaging with endogenous substances. Proc Natl Acad Sci U S A 100:10435–10439
65. Golman K, Olsson LE, Axelsson O, Mansson S, Karlsson M, Petersson JS (2003) Molecular imaging using hyperpolarized 13C. Br J Radiol 76:S118–S127
66. Ardenkjaer-Larsen JH, Fridlund B, Gram A, Hansson G, Hansson L, Lerche MH, Servin R, Thaning M, Golman K (2003) Increase in signal-to-noise ratio of > 10,000 times in liquid-state NMR. Proc Natl Acad Sci U S A 100:10158–10163
67. Matsuo M, Matsumoto S, Mitchell JB, Krishna MC, Camphausen K (2014) Magnetic resonance imaging of the tumor microenvironment in radiotherapy: perfusion, hypoxia, and metabolism. Semin Radiat Oncol 24:210–217
68. Day SE, Kettunen MI, Cherukuri MK, Mitchell JB, Lizak MJ, Morris HD, Matsumoto S, Koretsky AP, Brindle KM (2011) Detecting response of rat C6 glioma tumors to radiotherapy using hyperpolarized [1- 13C]pyruvate and 13C magnetic resonance spectroscopic imaging. Magn Reson Med 65:557–563
69. Albers MJ, Bok R, Chen AP, Cunningham CH, Zierhut ML, Zhang VY, Kohler SJ, Tropp J, Hurd RE, Yen YF, Nelson SJ, Vigneron DB, Kurhanewicz J (2008) Hyperpolarized 13C lactate, pyruvate, and alanine: noninvasive biomarkers for prostate cancer detection and grading. Cancer Res 68:8607–8615
70. Nelson SJ, Kurhanewicz J, Vigneron DB, Larson PE, Harzstark AL, Ferrone M, van Criekinge M, Chang JW, Bok R, Park I, Reed G, Carvajal L, Small EJ, Munster P, Weinberg VK, Ardenkjaer-Larsen JH, Chen AP, Hurd RE, Odegardstuen LI, Robb FJ, Tropp J, Murray JA (2013) Metabolic imaging of patients with prostate cancer using hyperpolarized [1-(1)(3)C] pyruvate. Sci Transl Med 5:198ra108
71. Zierhut ML, Yen YF, Chen AP, Bok R, Albers MJ, Zhang V, Tropp J, Park I, Vigneron DB, Kurhanewicz J, Hurd RE, Nelson SJ (2010) Kinetic modeling of hyperpolarized 13C1-pyruvate metabolism in normal rats and TRAMP mice. J Magn Reson 202:85–92
72. Aboagye EO, Bhujwalla ZM (1999) Malignant transformation alters membrane choline phospholipid metabolism of human mammary epithelial cells. Cancer Res 59:80–84
73. Glunde K, Bhujwalla ZM, Ronen SM (2011) Choline metabolism in malignant transformation. Nat Rev Cancer 11:835–848
74. van Sluis R, Bhujwalla ZM, Raghunand N, Ballesteros P, Alvarez J, Cerdan S, Galons JP, Gillies RJ (1999) In vivo imaging of extracellular pH using 1H MRSI. Magn Reson Med 41:743–750
75. Semenza GL (2012) Hypoxia-inducible factors: mediators of cancer progression and targets for cancer therapy. Trends Pharmacol Sci 33:207–214
76. Wilson WR, Hay MP (2011) Targeting hypoxia in cancer therapy. Nat Rev Cancer 11:393–410
77. Subarsky P, Hill RP (2003) The hypoxic tumour microenvironment and metastatic progression. Clin Exp Metastasis 20:237–250
78. Chaudary N, Hill RP (2007) Hypoxia and metastasis. Clin Cancer Res 13:1947–1949
79. Vaupel P, Kallinowski F, Okunieff P (1989) Blood flow, oxygen and nutrient supply, and metabolic microenvironment of human tumors: a review. Cancer Res 49:6449–6465
80. Lanzen J, Braun RD, Klitzman B, Brizel D, Secomb TW, Dewhirst MW (2006) Direct demonstration of instabilities in oxygen concentrations within the extravascular compartment of an experimental tumor. Cancer Res 66:2219–2223
81. Martinive P, Defresne F, Bouzin C, Saliez J, Lair F, Gregoire V, Michiels C, Dessy C, Feron O (2006) Preconditioning of the tumor vasculature and tumor cells by intermittent hypoxia: implications for anticancer therapies. Cancer Res 66:11736–11744

82. Pigott KH, Hill SA, Chaplin DJ, Saunders MI (1996) Microregional fluctuations in perfusion within human tumours detected using laser Doppler flowmetry. Radiother Oncol 40:45–50
83. Janssen HL, Ljungkvist AS, Rijken PF, Sprong D, Bussink J, van der Kogel AJ, Haustermans KM, Begg AC (2005) Thymidine analogues to assess microperfusion in human tumors. Int J Radiat Oncol Biol Phys 62:1169–1175
84. Nordsmark M, Bentzen SM, Rudat V, Brizel D, Lartigau E, Stadler P, Becker A, Adam M, Molls M, Dunst J, Terris DJ, Overgaard J (2005) Prognostic value of tumor oxygenation in 397 head and neck tumors after primary radiation therapy. An international multi-center study. Radiother Oncol 77:18–24
85. Peters KB, Brown JM (2002) Tirapazamine: a hypoxia-activated topoisomerase II poison. Cancer Res 62:5248–5253
86. Houghton PJ, Lock R, Carol H, Morton CL, Phelps D, Gorlick R, Kolb EA, Keir ST, Reynolds CP, Kang MH, Maris JM, Wozniak AW, Gu Y, Wilson WR, Smith MA (2011) Initial testing of the hypoxia-activated prodrug PR-104 by the pediatric preclinical testing program. Pediatr Blood Cancer 57:443–453
87. Wojtkowiak JW, Cornnell HC, Matsumoto S, Saito K, Takakusagi Y, Dutta P, Kim M, Zhang X, Leos R, Bailey KM, Martinez G, Lloyd MC, Weber C, Mitchell JB, Lynch RM, Baker AF, Gatenby RA, Rejniak KA, Hart C, Krishna MC, Gillies RJ (2015) Pyruvate sensitizes pancreatic tumors to hypoxia-activated prodrug TH-302. Cancer Metab 3:2
88. Kavanagh MC, Sun A, Hu Q, Hill RP (1996) Comparing techniques of measuring tumor hypoxia in different murine tumors: Eppendorf pO_2 Histograph, [3H]misonidazole binding and paired survival assay. Radiat Res 145:491–500
89. Hockel M, Vaupel P (2001) Tumor hypoxia: definitions and current clinical, biologic, and molecular aspects. J Natl Cancer Inst 93:266–276
90. Drevs J (2003) Soluble markers for the detection of hypoxia under antiangiogenic treatment. Anticancer Res 23:1159–1161
91. Le QT, Courter D (2008) Clinical biomarkers for hypoxia targeting. Cancer Metastasis Rev 27:351–362
92. Chapman JD (1979) Hypoxic sensitizers–implications for radiation therapy. N Engl J Med 301:1429–1432
93. Roels S, Slagmolen P, Nuyts J, Lee JA, Loeckx D, Maes F, Stroobants S, Penninckx F, Haustermans K (2008) Biological image-guided radiotherapy in rectal cancer: is there a role for FMISO or FLT, next to FDG? Acta Oncol 47:1237–1248
94. Mayr NA, Yuh WT, Jajoura D, Wang JZ, Lo SS, Montebello JF, Porter K, Zhang D, Mcmeekin DS, Buatti JM (2010) Ultra-early predictive assay for treatment failure using functional magnetic resonance imaging and clinical prognostic parameters in cervical cancer. Cancer 116:903–912
95. Newbold K, Castellano I, Charles-Edwards E, Mears D, Sohaib A, Leach M, Rhys-Evans P, Clarke P, Fisher C, Harrington K, Nutting C (2009) An exploratory study into the role of dynamic contrast-enhanced magnetic resonance imaging or perfusion computed tomography for detection of intratumoral hypoxia in head-and-neck cancer. Int J Radiat Oncol Biol Phys 74:29–37
96. de Bree R (2013) Functional imaging to predict treatment response after (chemo) radiotherapy of head and neck squamous cell carcinoma. Quant Imaging Med Surg 3:231–234
97. Tong T, Sun Y, Gollub MJ, Peng W, Cai S, Zhang Z, Gu Y (2015) Dynamic contrast-enhanced MRI: Use in predicting pathological complete response to neoadjuvant chemoradiation in locally advanced rectal cancer. J Magn Reson Imaging 42(3):673–680
98. Lawrence TS, Robertson JM, Anscher MS, Jirtle RL, Ensminger WD, Fajardo LF (1995) Hepatic toxicity resulting from cancer treatment. Int J Radiat Oncol Biol Phys 31: 1237–1248
99. Michalski JM, Gay H, Jackson A, Tucker SL, Deasy JO (2010) Radiation dose-volume effects in radiation-induced rectal injury. Int J Radiat Oncol Biol Phys 76:S123–S129
100. Sundgren PC, Cao Y (2009) Brain irradiation: effects on normal brain parenchyma and radiation injury. Neuroimaging Clin N Am 19:657–668

101. Hoskin PJ, Carnell DM, Taylor NJ, Smith RE, Stirling JJ, Daley FM, Saunders MI, Bentzen SM, Collins DJ, D'arcy JA, Padhani AP (2007) Hypoxia in prostate cancer: correlation of BOLD-MRI with pimonidazole immunohistochemistry-initial observations. Int J Radiat Oncol Biol Phys 68:1065–1071
102. Hallac RR, Zhou H, Pidikiti R, Song K, Stojadinovic S, Zhao D, Solberg T, Peschke P, Mason RP (2014) Correlations of noninvasive BOLD and TOLD MRI with pO_2 and relevance to tumor radiation response. Magn Reson Med 71:1863–1873
103. Jiang L, Weatherall PT, Mccoll RW, Tripathy D, Mason RP (2013) Blood oxygenation level-dependent (BOLD) contrast magnetic resonance imaging (MRI) for prediction of breast cancer chemotherapy response: a pilot study. J Magn Reson Imaging 37:1083–1092
104. Matsumoto A, Matsumoto K, Matsumoto S, Hyodo F, Sowers AL, Koscielniak JW, Devasahayam N, Subramanian S, Mitchell JB, Krishna MC (2011) Intracellular hypoxia of tumor tissue estimated by noninvasive electron paramagnetic resonance oximetry technique using paramagnetic probes. Biol Pharm Bull 34:142–145
105. Yasui H, Matsumoto S, Devasahayam N, Munasinghe JP, Choudhuri R, Saito K, Subramanian S, Mitchell JB, Krishna MC (2010) Low-field magnetic resonance imaging to visualize chronic and cycling hypoxia in tumor-bearing mice. Cancer Res 70:6427–6436
106. Matsumoto S, Batra S, Saito K, Yasui H, Choudhuri R, Gadisetti C, Subramanian S, Devasahayam N, Munasinghe JP, Mitchell JB, Krishna MC (2011) Antiangiogenic agent sunitinib transiently increases tumor oxygenation and suppresses cycling hypoxia. Cancer Res 71:6350–6359
107. Hou H, Dong R, Lariviere JP, Mupparaju SP, Swartz HM, Khan N (2011) Synergistic combination of hyperoxygenation and radiotherapy by repeated assessments of tumor pO_2 with EPR oximetry. J Radiat Res 52:568–574
108. Krishna MC, Matsumoto S, Yasui H, Saito K, Devasahayam N, Subramanian S, Mitchell JB (2012) Electron paramagnetic resonance imaging of tumor pO(2). Radiat Res 177:376–386
109. Matsumoto K, Subramanian S, Devasahayam N, Aravalluvan T, Murugesan R, Cook JA, Mitchell JB, Krishna MC (2006) Electron paramagnetic resonance imaging of tumor hypoxia: enhanced spatial and temporal resolution for in vivo pO_2 determination. Magn Reson Med 55:1157–1163
110. Subramanian S, Devasahayam N, Mcmillan A, Matsumoto S, Munasinghe JP, Saito K, Mitchell JB, Chandramouli GV, Krishna MC (2012) Reporting of quantitative oxygen mapping in EPR imaging. J Magn Reson 214:244–251
111. Matsumoto S, Hyodo F, Subramanian S, Devasahayam N, Munasinghe J, Hyodo E, Gadisetti C, Cook JA, Mitchell JB, Krishna MC (2008) Low-field paramagnetic resonance imaging of tumor oxygenation and glycolytic activity in mice. J Clin Invest 118:1965–1973
112. Hou H, Abramovic Z, Lariviere JP, Sentjurc M, Swartz H, Khan N (2010) Effect of a topical vasodilator on tumor hypoxia and tumor oxygen guided radiotherapy using EPR oximetry. Radiat Res 173:651–658
113. Hou H, Lariviere JP, Demidenko E, Gladstone D, Swartz H, Khan N (2009) Repeated tumor pO(2) measurements by multi-site EPR oximetry as a prognostic marker for enhanced therapeutic efficacy of fractionated radiotherapy. Radiother Oncol 91:126–131
114. Matsumoto K, English S, Yoo J, Yamada K, Devasahayam N, Cook JA, Mitchell JB, Subramanian S, Krishna MC (2004) Pharmacokinetics of a triarylmethyl-type paramagnetic spin probe used in EPR oximetry. Magn Reson Med 52:885–892
115. Gutte H, Hansen AE, Henriksen ST, Johannesen HH, Ardenkjaer-Larsen J, Vignaud A, Borresen B, Klausen TL, Wittekind AM, Gillings N, Kristensen AT, Clemmensen A, Hojgaard L, Kjaer A (2015) Simultaneous hyperpolarized (13)C-pyruvate MRI and (18) F-FDG-PET in cancer (hyperPET): feasibility of a new imaging concept using a clinical PET/MRI scanner. Am J Nucl Med Mol Imaging 5:38–45